The effect of yttrium additions on void swelling in liquid metal fast breeder reactor candidate cladding alloys

by

Richard Dean Hopson

A Thesis Submitted to the
Graduate Faculty in Partial Fulfillment of the
Requirements for the Degree of
MASTER OF SCIENCE

Major: Nuclear Engineering

Iowa State University
Ames, Iowa

1981

TABLE OF CONTENTS

I. INTRODUCTION

More than three decades ago the first nuclear reactor achieved a critical fission chain reaction beneath the Stagg Field football stadium at the University of Chicago. Since that time there has been a worldwide effort to harness the enormous energy contained within the atomic nucleus for the peaceful use of nuclear energy. This has led to the development of numerous types of nuclear reactors for electrical power production.

Electrical power production, previous to the discovery of the first critical chain reaction until today, has depended chiefly upon coal and oil as fuel sources. Worldwide demands on coal and oil for energy production have consumed large amounts of energy sources once believed inexhaustible. The advent and development of nuclear energy have lessened the severity of the rate at which coal and oil are being consumed, thus "buying time" to develop new energy sources. Many think that our nuclear fission fuels also stand the chance of becoming critically short if ways of either renewing or discovering alternative energy sources are not found.

Billions of dollars are being spent on research programs to insure that the world does not "freeze to death in the dark". These programs are investigating fast breeder reactors, controlled thermonuclear fusion reactors, geothermal power, solar power, and many others. Most technologically advanced nations have recognized the nuclear option and have placed it high on their priority list. Current

trends in the technology of power production suggest the fast breeder reactors will provide an economical energy source in the near future.

The liquid metal fast breeder reactor (LMFBR) concept is to fuel the reactor with ^{239}Pu and ^{238}U and then "breed" or produce directly ^{239}Pu, the fuel needed for future operations. A typical breeding ratio (BR) for a LMFBR would be BR≈1.2-1.5, where BR equals the ratio of the number of fissile atoms produced to the number consumed (1). This BR would lead to a doubling time of approximately seven years. Doubling time is the time to double the number of fissile atoms. Since breeder reactors produce more fuel than is consumed, one can see that they may help meet the world's demand for a renewable energy source.

The LMFBR has been in existence since 1951. Since that time numerous engineering problems have been solved; however, there is always the question, "How can the system be improved?" Researchers and engineers are constantly striving to increase the breeding ratio, thus shortening the doubling time. This is extremely important from an economical standpoint. Increasing the breeding ratio means making maximum use of neutrons toward the production of new fissile atoms (i.e., ^{239}Pu). Therefore, a need exists for coolants and structural materials that will not thermalize or otherwise adversely affect the fast neutron population. Structural materials would have to be kept to a minimum without endangering their ability to withstand the stresses and environment within the reactor core. One particularly important consideration is the effect of neutron irradiation in producing void swelling in cladding and duct materials.

Fast breeder reactors' cladding and duct materials will be exposed to fast neutron fluences of $(2-3)\times10^{23}$ n/cm^2 (E>0.1 MeV). These fluences would induce approximately 18% swelling at peak swelling temperatures in 20% cold worked 316 stainless steel (2). (316 stainless steel is currently being used as the cladding and duct material in experimental fast breeder reactors.) To find ways of controlling void swelling, commercial and candidate structural materials need to be exposed to fluences expected in commercial fast breeder reactors. At the Experimental Breeder Reactor (EBR-11), a fluence of $10^{23} n/cm^2$ would take between 2-3 years. Valuable research time and money would be consumed in this period. Therefore, a more economical means of producing the same amount of radiation damage would be very useful.

A possible solution to this dilemma is heavy ion bombardment. As can be seen below, heavy ion bombardments can produce 100 displacements per atom (dpa) in approximately 5 hours. Thus, damage rates with heavy ions (20 dpa/hr) are much larger than those in fast reactors (0.0035 dpa/hr). Heavy ion bombardment has proven to be a valuable technique toward contracting the scale for the study of void swelling in fast reactor structural materials.

While swelling, void densities, and void diameters were found to be similar both in ion and fast neutron damaged commercial Fe-Cr-Ni alloys (3), other evidence indicates that the techniques used to establish these similarities are limited to only certain alloys. As an example, Rowcliffe et al. (4) found that the precipitate microstructure formed in 316 stainless steel during neutron irradiation

was unstable during subsequent ion bombardment; consequently, the relative swelling rates at various temperatures were not correctly simulated. Although differences exist, there is still a strong contention that ion bombardment techniques should be used for the initial evaluation of the effects of irradiation induced defects in candidate cladding and duct materials.

Candidate LMFBR cladding and duct alloys Fe-26%Ni-9%Cr[1] (here designated AL1) and Fe-35%Ni-12%Cr (AL2) are among those being considered for use in commercial fast reactors (5). Research on these two alloys consists of mechanical property studies and the effects of fast neutron irradiation. The effects of minor additions of rare-earth metals upon structural steel for reactor applications have been published (6, 7, 8). These publications deal primarily with changes in mechanical and corrosion properties upon adding rare-earth elements. Very little, if any, published research has been done on the effects of additions of rare-earth metals on void swelling. In general, making minor alloying additions enhances certain properties while degrading others. The ideal condition would be the enhancement of all properties, but this is rarely the case. A desired balance must be struck. As an example, in austenitic stainless steels, swelling varies systematically with the Cr and Ni content (9). Generally as the Ni content increases, swelling decreases for a given Cr concentration and as the Cr content increases, swelling increases for a given Ni concentration.

---

[1]Unless otherwise indicated, concentrations are given in weight percent.

Ni is an austenizer and with proper heat treatment provides strength and ductility in steels. Cr is a ferritizer and provides high corrosion resistance to steels. Considering these and other features, where is the line drawn? This question is answered based on the environment in which the material is used. The same type of decision must also be made toward minor alloying with rare-earth metals.

Published works on high-temperature oxidation of Fe-Cr-Y alloys imply that yttrium additions to austenitic steels increase oxidation resistance (6). Also, it is anticipated that yttrium additions ($\sim$1.0 wt. %) to 20/25 Nb steel lend greater adhesions of surface oxide. Left unanswered are the effects of small yttrium additions (0.1-0.2%) upon void swelling in austenitic steels. This unknown will be addressed to the AL1 and AL2 alloys in the remainder of this thesis.

II. VOID SWELLING

A. Introduction

The study of void formations due to neutron irradiation is a relatively new field of research. Voids were first observed and reported by Cawthorne and Fulton in 1966 (10). This detection of voids prompted numerous studies to define the mechanisms by which voids are produced. Based on these investigations, researchers began the tedious process of trying to define models by which radiation induced void swelling may be predicted (11). A review of the advances in void swelling theory is given by Mansur and Yoo (12) in which are discussed (a) the development of a cascade diffusion theory, (b) the effects of mobile helium on void growth, and (c) spatial variations in swelling during ion bombardment. This publication along with other works by Johnston et al. (9), Wiedersich (13), and others have provided designers with information by which void swelling may be controlled.

One of the important effects of radiation damage in fast reactor structural metals is void swelling. The designer must compensate for metal swelling by increasing the distance between fuel pins to provide adequate coolant flow and, more importantly, the freedom of control rod movement. An increase in fuel pin spacing leads to a lower breeding ratio and power density, which adversely affects the economics of power production employing fast breeder reactors. Factors to be considered in the design of fast breeder reactors based on swelling in reactor metals have been published by Huebotter and Bump (14).

B. Defect Clustering, Void Formation, and Swelling

Steady-state defect concentrations (i.e., vacancies and interstitials) may be obtained by reaction-rate equations analogous to those used in chemical kinetics (13). These equations were extensively used by Damask and Dienes in the development of the annealing theory of radiation-induced point defects (15). Point defects were assumed to be produced at random within the solid. They moved by a random-walk process through a crystalline material until they were annihilated by recombination with an opposite type of defect (i.e., vacancy with interstitial) or by annihilation at fixed lattice sinks, such as dislocations, voids and grain boundaries. The effects of spatial variations and defect clustering in cascades are neglected for simplicity. A more detailed account of void swelling including these factors has been published (12). These simplifications, however, do not induce errors that would make the Damask and Dienes analysis invalid (13).

The rate of change of the number of vacancies, dN_v/dt, is given by Wiedersich (13) as:

$$\frac{dN_v}{dt} = N_{pv} - \nu_v N_v a_v C_v - \nu_i N_i a_i C_i - \nu_v N_v P_v \qquad [1]$$

The subscripts v and i indicate vacancies and interstitials, respectively. N_{pv} is the total production rate of vacancies, and ν_v and ν_i are jump frequencies. C_v and C_i are atomic fraction, N_v and N_i are the total number of vacancies and interstitials and a_v and a_i are the

geometrical factors corresponding to the recombination volume. Also, P_v is the probability that a single jump of a vacancy results in annihilation at a sink. $\nu_v N_v a_v C_i$ = the loss rates of vacancies caused by vacancies jumping into a_v sites around an interstitial. $\nu_i N_i a_i C_v$ = the vacancy loss due to recombination of moving interstitials with stationary vacancies. $\nu_v N_v P_v$ = vacancy loss by annihilation at sinks. For convenience and symmetry, equation [1] is divided by the total number of lattice sites yielding

$$\frac{dC_v}{dt} = n_{pn} - (\nu_v a_v + \nu_i a_i) C_v C_i - \nu_v P_v C_v \qquad [2]$$

where all concentrations are now in atomic fractions, and the production rate, n_{pv}, is in atomic fractions per unit time. Equation [2] can be modified to express changes in interstitial concentrations by interchanging v and i subscripts. The total probability, P_v, is different from P_i because of differences in interactions of interstitials and vacancies with various sinks.

Wiedersich (13) also gives an expression similar to [2] which includes the thermal equilibrium concentrations of vacancies and interstitials, C_v^{th} and C_i^{th} as follows:

$$\frac{dC_v}{dt} = n - (\nu_i a_i + \nu_v a_v)(C_v C_i - C_v^{th} C_i^{th}) - \nu_v P_v (C_v - C_v^{th}) \qquad [3]$$

and a similar expression for $\frac{dC_i}{dt}$ as follows:

$$\frac{dC_i}{dt} = n-(\nu_v a_v + \nu_i a_i)(C_i C_v - C_i^{th} C_v^{th})-\nu_i P_i (C_i - C_i^{th}) \qquad [4]$$

where: $n = n_{pv}-n_{pv}^{th} = n_{pi}^{th}-n_{pi}^{th}$, is the radiation induced defect production rate.

$(\nu_v a_v + \nu_i a_i)(C_i C_v - C_i^{th} C_v^{th})$ is the net loss of defects by recombination.

$\nu_v P_v (C_v - C_v^{th})$ and $\nu_i P_i (C_i - C_i^{th})$ are the net losses to sinks of vacancies and interstitials, respectively.

When steady-state conditions are reached, the time derivatives in equations [3] and [4] are zero. The difference of the equations yields a relationship between the steady-state interstitial and the vacancy concentrations

$$\nu_i P_i (C_i - C_i^{th}) = \nu_v P_v (C_v - C_v^{th}). \qquad [5]$$

By letting $(C_i - C_i^{th}) = \Delta C_i$ and $(C_v - C_v^{th}) = \Delta C_v$, the rate of annihilation at sinks of radiation-produced defects can be given by

$$R = \nu_i P_i \Delta C_i = \nu_v P_v \Delta C_v. \qquad [6]$$

Equation [6] implies that, during steady-state, equal numbers of interstitials and vacancies must be annihilated at sinks; however, steady-state conditions are rarely encountered. Sinks present within the material exhibit a bias for capturing one type of defect. The most obvious sink to discriminate between vacancies and interstitials is dislocations. Dislocations interact more strongly with inter-

stitials because interstitials distort the surrounding lattice more than vacancies do.

The differences in interactions of interstitials and vacancies (the bias) for the different types of sinks are taken into account by assigning individual annihilation probabilities P_i^k and P_v^k, where the superscripts identify the type of sink while the subscripts identify the type of defect. The total loss rates of vacancies and interstitials at sinks (last terms in equations [3] and [4]) can be expanded with $P_v \equiv \Sigma_k P_c^k$ and $P_i \equiv \Sigma_k P_i^k$ as

$$R_v = \nu_v P_v \Delta C_v = \nu_v \Delta C_v P_v^v + \nu_v \Delta C_v \sum_{k \neq v} P_v^k \qquad [7]$$

$$\text{and } R_i = \nu_i P_i \Delta C_i = \nu_i \Delta C_i P_v^v + \nu_i \Delta C_i \sum_{k \neq v} P_i^k \qquad [8]$$

where the loss rates to voids are given on the far right sides. Subtraction of the last two terms of equations [7] and [8] gives

$$\delta = \nu_i \Delta C_i \sum_{k \neq v} P_i^k - \nu_v \Delta C_v \sum_{k \neq v} P_v^k \qquad [9]$$

which is the net rate of precipitation of interstitials at all sinks other than voids. Fractional volume increases, $\frac{\Delta V}{V}$, in materials are caused by excess interstitial precipitation, not void formation (13). In fact, small volume increases are expected when interstitials have enough mobility to be annihilated at sinks and vacancies do not.

Radiation-induced displacement concentrations cause significant and lasting microstructural changes in metals. Void swelling is one such important change that occurs during elevated-temperature irradi-

ation. In addition to displacement damage, a more complex nucleation problem is encountered as a result of the (n, α) reaction. The insoluble transmutation product, helium, precipitates into void embroys. Helium can increase the void-nucleation rate dramatically when the helium flux to void embryos is equal to or larger than the vacancy flux (13).

C. Damage Produced by Ion Bombardment

In the context of LMFBR's, the economics of nuclear power production requires that the fuel and related cladding duct material remain in service for fluences in excess of 10^{23} neutrons/cm^2 (i.e., exposed to fluxes of about 10^{16} neutrons/cm^2 sec for a period of 1 year) (16). In currently available irradiation facilities it takes in excess of one year to achieve these fluences. There is, therefore, a great need to devise irradiation tests that can produce the required irradition damages in a short period of time (such as days).

Heavy-ion bombardment of materials has proven to be such a tool (16, 17, 18). Heavy- and light-ion beam currents with energies from approximately 1 to 10 MeV can be obtained in accelerators. The initial energy of ions is dissipated in solids at short ranges, typically shorter than 10 μm. Incident ion energies are normally in the MeV range; thus, the principal energy loss mechanism of the incident ion at a given depth of penetration is electron excitation (16). The atomic stopping power absorbs the remainder of the ion's energy.

The electronic stopping power is given by the following equation (16):

$$\left(\frac{dE}{dx}\right)_e = -KE^{\frac{1}{2}}, \quad K = 0.3[(eV)^{\frac{1}{2}}/\mathring{A}] \times N\mathcal{Z}^{2/3} \qquad [10]$$

where: E is the incident particle energy, x is the path length, the subscript e refers to the electron, N is the density of the target particles in $(\mathring{A})^{-3}$, and $\mathcal{Z}$ is the atomic number of the atoms of the target material. The equation for the atomic stopping power is given by the following (16):

$$\frac{dE}{dx} = N\int_{T_o}^{T_m} \sigma T\,(E,T)dT \qquad [11]$$

where T is the energy transferred to the lattice atom, T_m is the maximum energy transferable to a lattice atom, T_o is the minimum energy transferred to the lattice atom and $\sigma(E,T)dT$ is the differential cross section for transferring energies between T and T + dT to a lattice atom by an incident particle of energy E. Integration of the electronic stopping power equation (eg. [10]) gives the ion energy at depth x

$$E(x) = [(E_o)^{\frac{1}{2}} - \tfrac{1}{2}Kx]^2 \qquad [12]$$

where E(x) is the energy of the bombarding ion at depth x and E_o is the initial energy of the bombarding ion.

Although the question of how and where the impinging ion's energy is lost is important, the rate at which displacements are produced in reactor structural metals is of greater importance in comparing the effects of neutron and ion irradiations. This comparison is dealt with in detail by Mansur and Yoo in (12) and Mansur in (19).

An expression for the rate at which lattice atom displacements at depth x are produced is given by Olander (16) as follows:

$$R_d(x) = NI \int_{T_d}^{\Lambda_E} \sigma(E,T)\ \nu(T)dT,\ \frac{\text{Displaced Atoms}}{\text{cm}^3\ \text{sec}} \qquad [13]$$

where N is the atom density of the target particle, I is the ion current density or ion flux in units of ions/cm^2 sec, x is the path length, T_d is the threshold displacement energy, $\nu(T)$ is the number of displaced atoms for each collision that produces a primary knock-on atom of energy T, $R_d(x)$ is the lattice atom displacement rate at depth x, and Λ is given by

$$\Lambda = \frac{4M_1M_2}{(M_1+M_2)}\ 2$$

where M_1 and M_2 are the masses of the incident particle and target atom, respectively.

Multiplication of R_d in equation [13] by the irradiation time and division by the lattice density, N, gives the number of displacements per lattice atom for irradiation to a given fluence (It).

$$C_d = \text{number of displacements/atom} = It \int_{T_d}^{\Lambda_E} \sigma(E,T)\ \nu(T)dT \qquad [14]$$

It is seen from equation [14] that displacement concentrations depend on the ion beam intensity (ion flux) and the duration of exposure to the ion beam. For Ni^+ ions, beam intensities on the order of 10^{13} ions/cm^2 sec can be achieved (16). Figure 1 shows that the displacement rate for 5 MeV Ni^+ ions ranges up to about 10^{-2} dpa/sec. By comparison, the calculated displacement rate for a fast-neutron flux of $\sim 10^{15}$

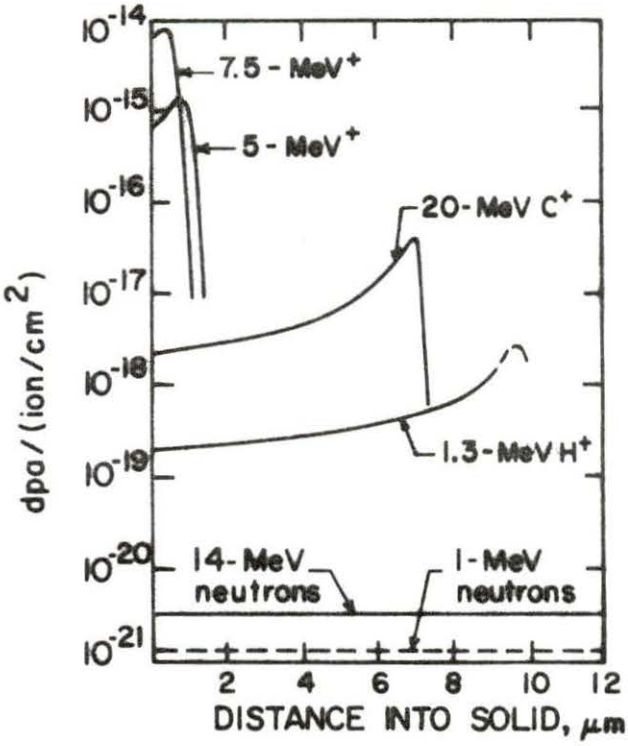

Figure 1: Displacement-damage effectiveness as a function of penetration depth for ions impinging on nickel. [From Ref. (16)].

neutrons/cm^2 sec is above 5 x 10^{-6} dpa/sec. This comparison shows that the same number of displacements per atom are produced in about 5.2 hours of 5 MeV nickel ion bombardment as is produced by approximately one year of 14 MeV neutron irradiation.

As a result of these time savings and the ability to simulate, in some respects, fast neutron irradiation damage by ion bombardment, studies in LMFBR candidate cladding alloys AL1 and AL2 were conducted by use of 4 MeV $^{56}Fe^{2+}$ ions. The simultaneous implantation of 0.4 MeV $^{4}He^{+}$ ions was also used to simulate the helium build-up due to the (n, α) reaction.

III. EXPERIMENTAL PROCEDURES

A. General

The Fe-Ni-Cr alloys were supplied by The Hanford Engineering Development Laboratory (HEDL). The chromium and nickel concentrations of the starting alloys are given in Table 1. Sheet samples were prepared and bombarded by 4 MeV $^{56}Fe^{2+}$ ions only and by a dual beam of 4 MeV $^{56}Fe^{2+}$ and 0.4 MeV $^{4}He^{+}$ ions. Portions of these alloys were doped with 0.1 wt percent of yttrium to study its effects upon void swelling. Each material (AL1 and AL2, doped and undoped) was irradiated at several temperatures to a single displacement concentration of 100 dpa. The 0.4 MeV $^{4}He^{+}$ ions were simultaneously implanted at a rate of 0.7 appm per dpa. This is in close agreement with helium production rates found in like alloys (i.e., 316SS, PE-16, INCONEL -600) exposed to the EBR-II environment for one year (20).

B. Sample Preparation

Samples of AL1 and AL2 were taken from the bar stock supplied by HEDL and arc melted into doped (0.1 wt % Y) and undoped 60 gram fingers approximately 4 inches long and 0.5 inches in diameter. After arc melting, each finger was weighed and ultrasonically cleaned in a solution of 95 ml HNO_3 and 5 ml HF to remove any surface contaminants. The fingers were given a homogenizing anneal for 16 hours at 1150°C in a vacuum of 10^{-6} torr. The fingers were then sectioned according to Figure 2. It is important to section the fingers after the homogenizing

Table 1. Chromium and nickel concentrations of the starting alloys as recorded on the Certificate of Test for as-received bar stock

	D21	D68
Cr	8.68	11.83
Ni	25.71	35.21

anneal to eliminate or minimize any existing component concentration gradient within the material. Combustion technique and wet chemical analyses were conducted on piece #6 of each sample to determine carbon and yttrium content (Table 2).

Table 2. Wet and combustion chemical analysis of piece #6 (see Figure 2) undoped and doped AL1 and AL2 samples after a homogenizing anneal for 16 hours at 1150°C in a vacuum of about 10^{-6} torr

Sample	C	Y
AL1	0.0468	0.00
AL1 + 0.1% Y	0.0480	0.07
AL2	0.0350	0.00
AL2 + 0.1% Y	0.0357	0.09

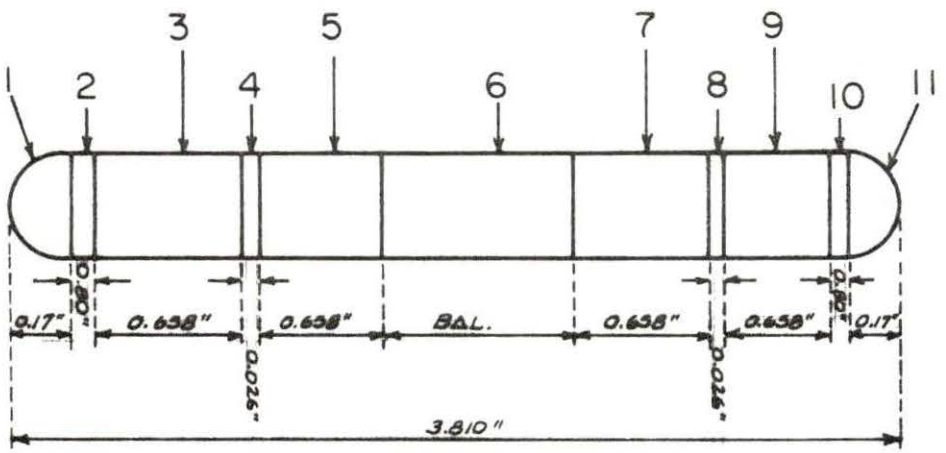

Figure 2: An example of an arc melted finger cutting schedule for AL1 and AL2 alloys.

Piece #9 of each sample was cold rolled to sheet stock approximately 0.02 inches thick. This thickness was sufficient to provide enough extra surface material for polishing to an acceptable finish leaving 0.014 inches thickness (0.014 inches is the optimum thickness for the sample holder used during ion bombardment in ORNL's Van de Graaff dual beam accelerator). Sheet stock preparation involved a series of cold rolling, and between each rolling an intermediate recrystallizing anneal for one hour at 1150°C in a vacuum of about 10^{-6} torr. Care was taken during the rolling process not to have area reduction in excess of roughly 30 percent in order to avoid cracking. In order to determine a final annealing time and temperature, piece #5 of each sample was reduced to sheet stock exactly as described above. One centimeter squares were cut from the sheet stock. One square from each sample was annealed for seven hours at 1150°C in a vacuum of about 10^{-6} torr. Each sample was then electrolytically polished for one and one-half minutes in a 6% perchloric acid and 94% methanol alcohol solution at -70°C with 50 volts applied. After polishing, each sample was electrolytically etched in a solution of 10% oxalic acid and water for about one minute with 6 volts applied. Micrographs were prepared from each annealed and as-rolled sample. It was found that the final anneal time and temperature provided full recovery and recrystallization without significant grain growth (Figure 3).

Discs 1/8 inch in diameter were punched from the 20-22 mil-thick sheet stock. The discs were ultrasonically cleaned in acetone, rinsed in distilled water, and again ultrasonically cleaned in methyl alcohol

Figure 3: Micrographs of AL1 and AL2, undoped and doped samples showing the results of the final anneal for 7 hrs at 1150°C in a vacuum of 10^{-6} Torr.

(a) cold rolled AL1 (100X)

(b) AL1 annealed at 1150°C for 7 hrs after cold rolling (100X)

(c) AL1 + 0.1 % Y annealed at 1150°C for 7 hrs after cold rolling (100X)

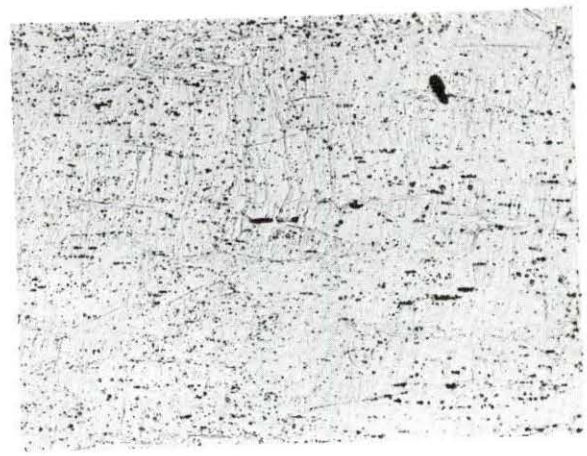

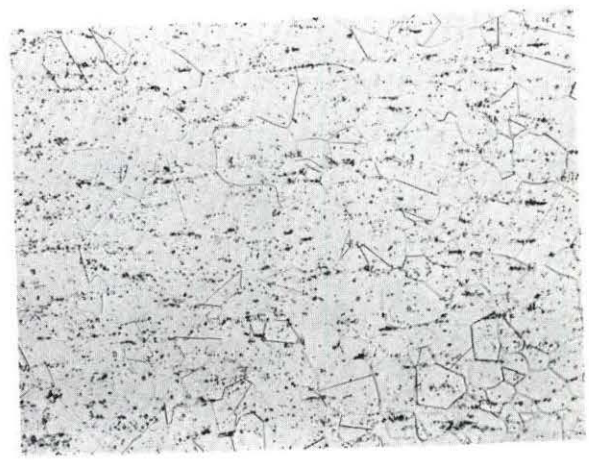

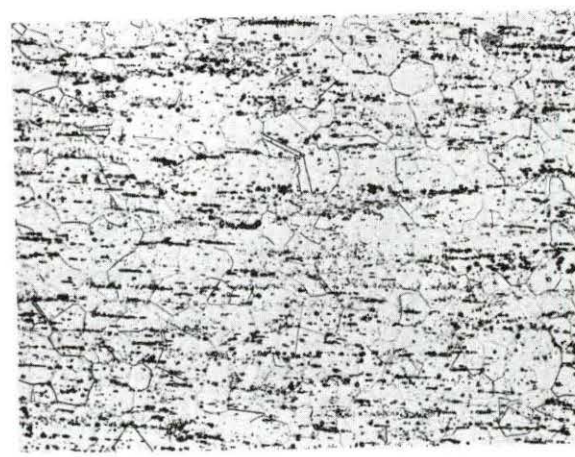

Figure 3: (continued)

(d) AL2 annealed at 1150°C for 7 hrs after cold rolling (100X)

(e) AL2 + D.1 % Y annealed at 1150°C for 7 hrs (100X)

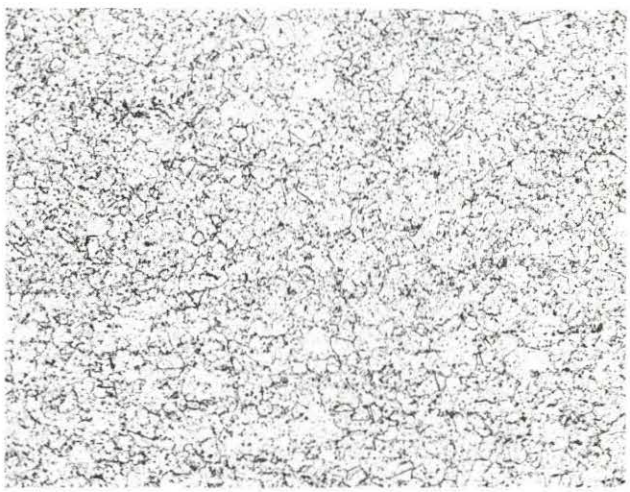

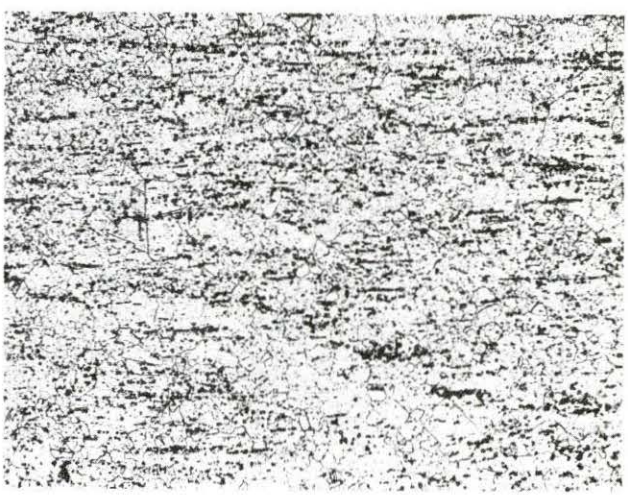

and blown dry. An anneal for one hour at 1150°C in a vacuum of about 10^{-6} torr was conducted to provide recovery and recrystallization from lattice damage that might have been induced while punching. The disc samples were segregated into groups of ten discs according to sample type and cemented to a polishing block (Figure 4). The bonding cement (adhesive) used to fix the samples to the polishing block was Lakeside 70 Mounting Cement marketed by Buehler Ltd. The polishing block dimensions and material were selected to provide enough weight or downward force for polishing without hand manipulation. The discs were polished on one side with 600 grit carbon-silicon paper using a Buehler polishing apparatus (catalog #151153) until flat (0.002-0.003 inches removed). The samples were ultrasonically cleaned in distilled water (acetone and methyl alcohol will soften or remove the adhesive) to remove any foreign particles left by the 600 grit paper before advancing to the next polishing stage. The next stage was conducted by placing the polishing block with samples attached, face down, in a Syntron polisher employing a wax lap and Linde A (0.3 μm, Al_2O_3) polishing compound for four hours (or until abrasions left by the 600 grit paper were removed). After the Linde A polishing, the specimens were removed from the polishing block, ultrasonically cleaned in distilled water, turned polished-side down, and remounted on the polishing block by the method previously stated. The sides of the discs that have thus far been polished (the back sides) will be placed against the thermalizer block of the target assembly in the Van de Graaff accelerator. Polish-

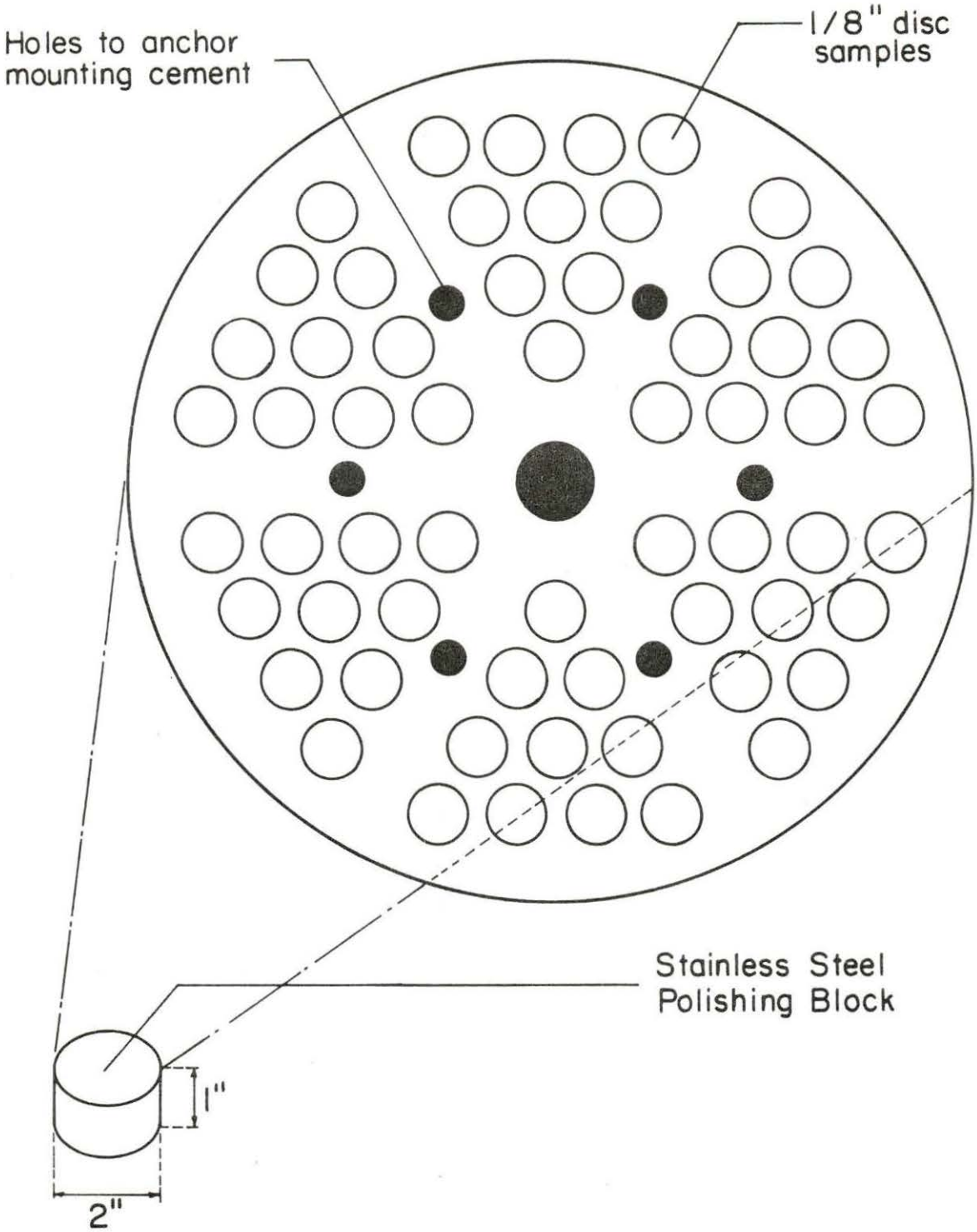

Figure 4: The arrangement in which samples we placed on a polishing block for surface preparation of samples to be used for ion bombardments.

ing the back side of the sample provides good thermal contact for heating the sample during elevated temperature ion bombardment.

To polish the front side (side to face the ion beam), the processes of polishing with the 600 grit paper and Linde A compound were repeated. After polishing with the Linde A polishing compound, the polishing block and samples were ultrasonically cleaned in water to remove any remaining Linde A compound, then placed face-side down in the Syntron polisher. For this polishing Linde B (0.05 μm, Al_2O_3) polishing compound and cloth lap ("microcloth") were employed for about 20 minutes. Linde B compound should be used for the shortest period of time possible to remove the abrasions left by the Linde A compound. Extended use of Linde B compound on these alloys results in unwanted surface relief. The objective of polishing samples for ion bombardment is to provide as smooth and flat a surface as possible, preferably optically smooth and flat so as not to produce geometries that are unsuitable for making swelling analyses. This is extremely important when the method of swelling analysis includes the use of an interferometer or profilometer instrument.

One might suggest a slight electropolish to remove the last little bit of cold work left by the Linde B compound, thus providing a smoother surface. This suggestion was tried on these alloys and resulted in unsatisfactory surfaces. The electropolishing consisted of removing 2-3 μm of surface material by a 10 sec polish at 20°C and 275 milliamps of current in a 1 to 7 parts sulfuric acid-methanol solution. Because these alloys are two-phase alloys, electropolishing only enhances the unwanted surface relief. Surface topography after each polishing step

is exhibited in Figure 5. Electropolishing techniques suggested by Lee and Rowcliffe (21) would prove useful for post-ion bombardment analysis, but are of little use for pre-bombardment electropolishing when final analysis of swelling is to be done by interferometer or profilometer instruments on two-phase alloys. The effects of electropolishing an AL1 sample are seen by compariing Figure 5C to Figure 6.

Once all surface preparations were complete, each sample was examined in an optical microscope for any material defects that would adversely affect the uniformity of the ion beam penetration (i.e., cracks, scratches, imbedded particles from polishing compounds, bonding cement, etc.). Satisfactory samples were placed in suitable containers for insuring ease in identification and protection from an environment that might otherwise damage the sample.

C. Ion Bombardment

All the suitable samples of AL1 and AL2, doped and undoped, were bombarded at the Oak Ridge National Laboratory (ORNL) with heavy-ions only and with heavy-ions and helium simultaneously. The "dual beam" technique or irradiation is used because fast neutrons within reactors not only produce displacements, but also helium as a result of (N, α) reactions. Analytical investigations (17, 22) have shown that void growth is affected by the presence of helium. This implies that helium must be implanted into the metal either prior to or during heavy-ion bombardment to simulate properly the effect of neutron irradiation.

The Van de Graaff dual beam accelerator (Figure 7) was developed for the purpose of more closely imitating the effects of neutron-

Figure 5: Appearance of the surface of a AL1 sample after each stage of polishing with various polishing compounds.

(a) AL1 1/8" disc polished with 600 Grit carbon-silicon paper (50X)

(b) AL1 1/8" disc polished for 4 hrs with Linde A polishing compound following the 600 Grit polish (400X)

(c) AL1 1/8" disc polished for 20 min with Linde B polishing compound following the Linde A polish (400X)

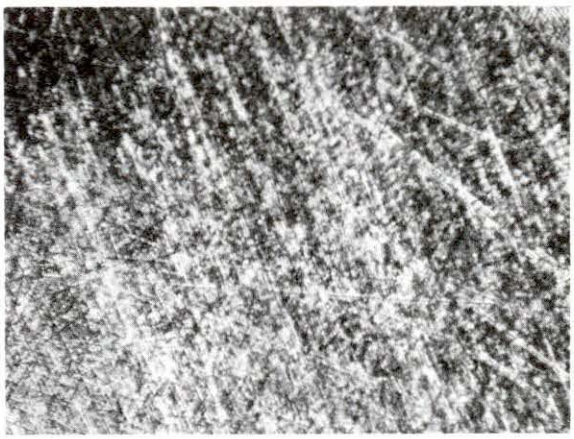

Figure 6: AL1 1/8 inch disc sample electropotished for 10 sec. at 20°C and 250 MA. of current in a solution of 1 to 7 parts sulfuric acid and methanol following the Linde B polish (50x).

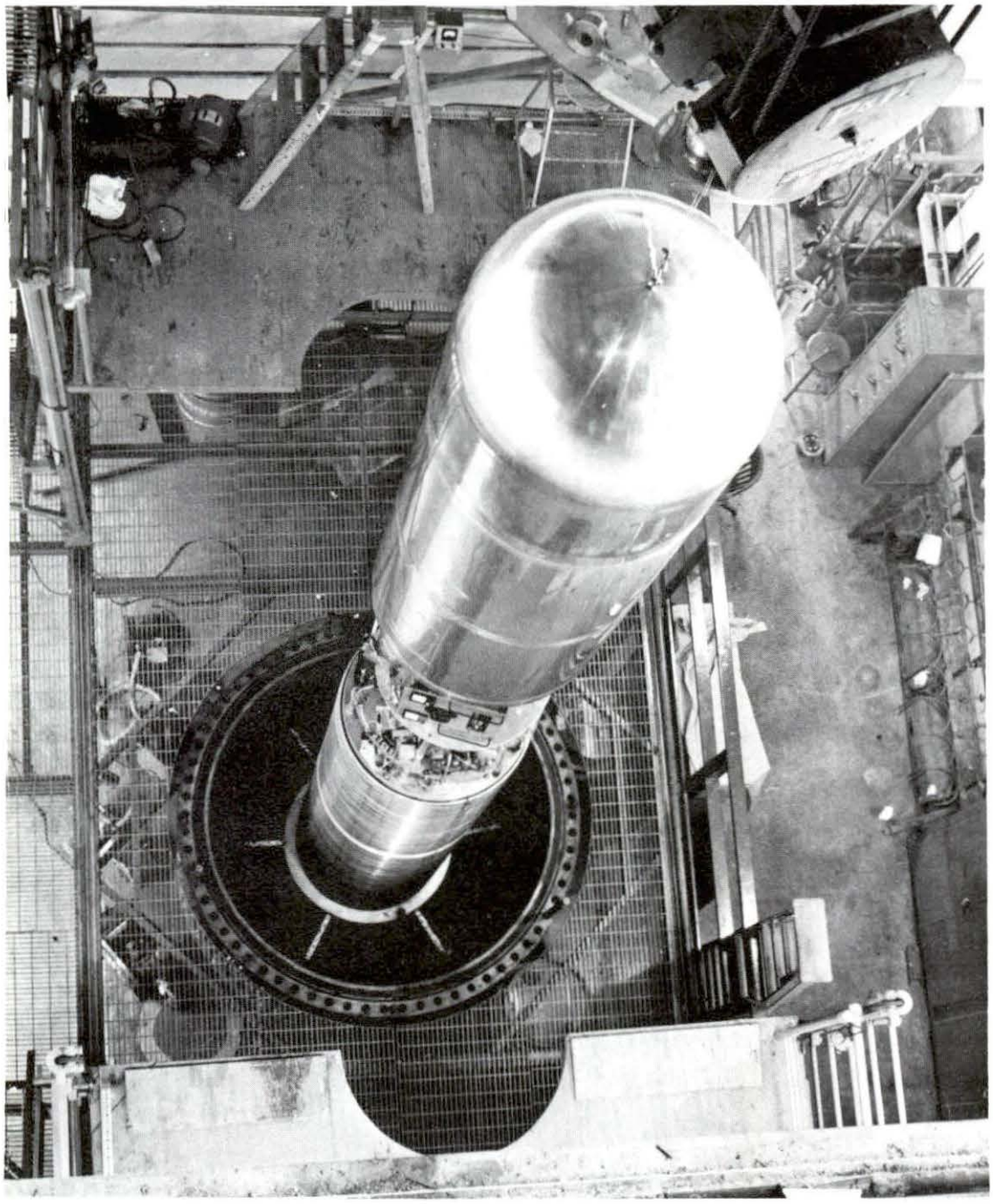

Figure 7: View of the upright tank and enclosed electrical components of the heavy-ion Van De Graaff accelerator at ORNL.

induced damage in reactor materials. The facility at ORNL can simultaneously bombard samples with heavy ions and light ions like helium. The ion beams can be made to impinge upon nine target samples at the same time in a continuous or pulsed (chopped) mode (17). Sample temperatures can be accurately measured and the target environment monitored with a residual gas analyzer. Helium penetrations take place over a broad depth by varying the helium ion energy. An overall view of the accelerator beam lines is given in Figure 8. For more detailed information concerning the ORNL dual beam Van de Graaff accelerator, the reader is referred to references (17) and (18).

Of primary interest at this point is the damage chamber (item K, Figure 8) and related equipment. An expanded view of the chamber is shown in Figure 9. The target assemblies (Figure 10) have six individual target heater modules, large bellows, which permits 230 mm of linear motion, and all the power and instrumentation feed-throughs. A precision machined bed attached to the chamber body is used for aligning any desired target with the intersection point of the two charged beams. The heavy ion and light ion beams enter the chamber by separate ports with a 15° angle between them. Other ports in the chamber permit illumination and visual observation of the samples during bombardment.

Figure 11 gives a view of a target assembly with each of the six specimen holder-heater modules (item a) in progressive stages of assembly. The heaters are dispenser cathode triode-type Y646B electron gun assemblies (item b). The electron guns operate with the cathode drawing about 10 milliamps at 600 to 800 volts negative to ground,

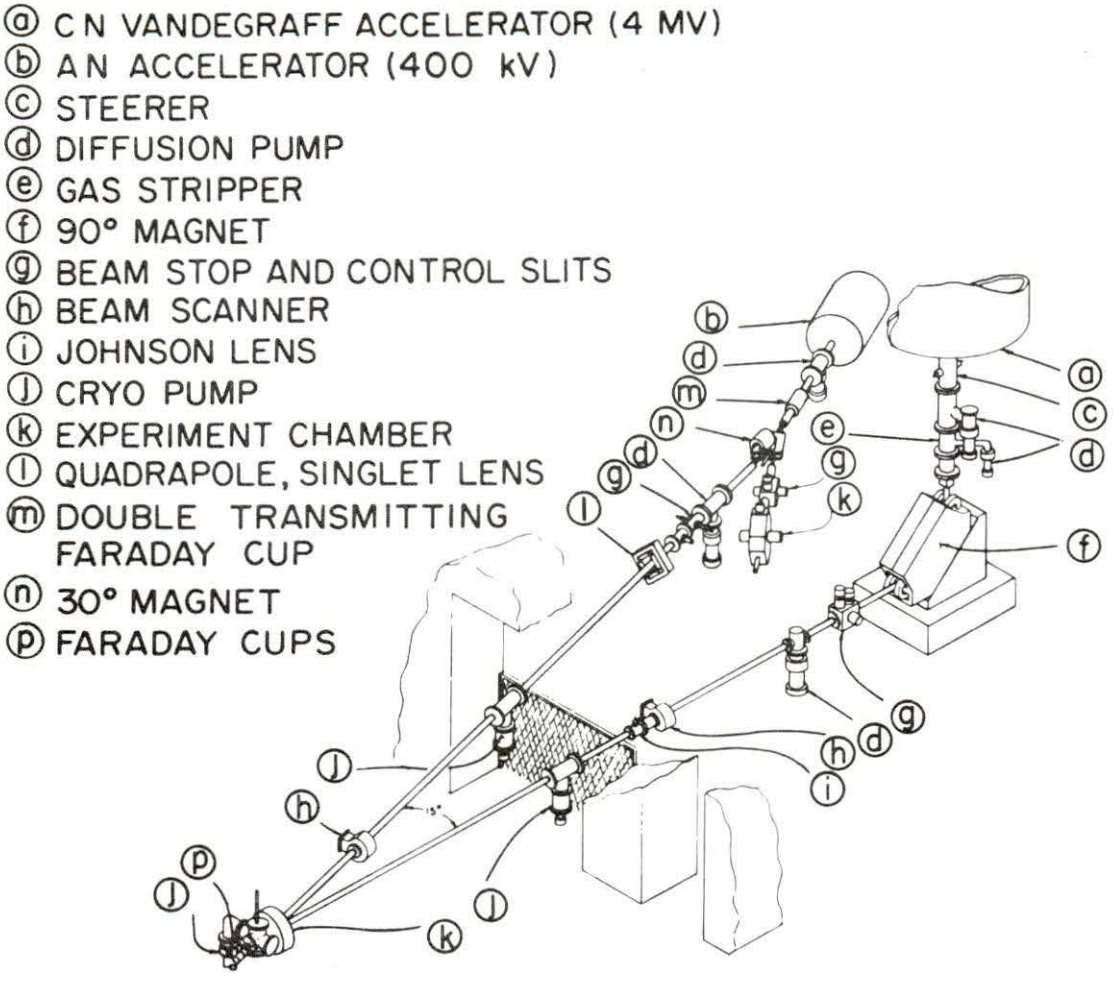

Figure 8: Schematic of the two accelerators and their respective beam lines to the Radiation Damage Target Chamber (lower left). (From Ref. 18)

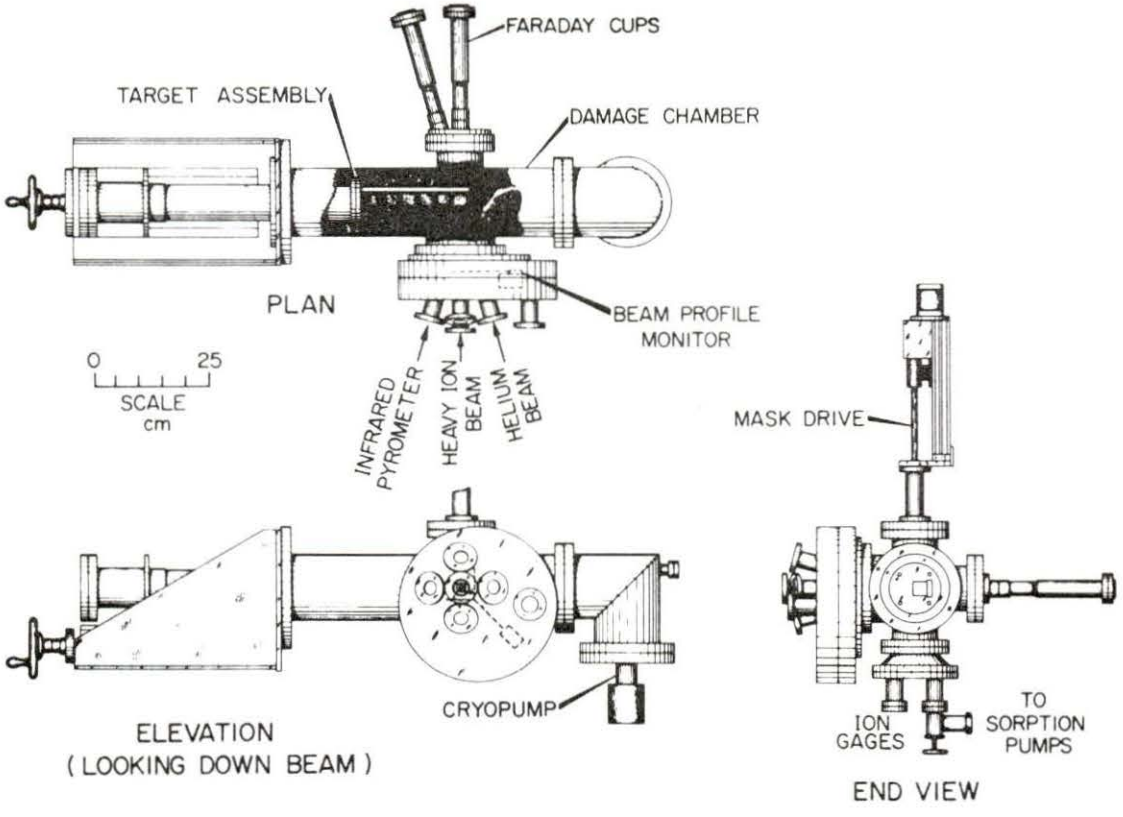

Figure 9: Layout of the Radiation Damage Target Chamber of the Van de Graaff dual beam accelerator at ORNL. (From Ref. 18)

Figure 10: Target assembly with electrical feed through components of the Van de Graaff dual beam accelerator.

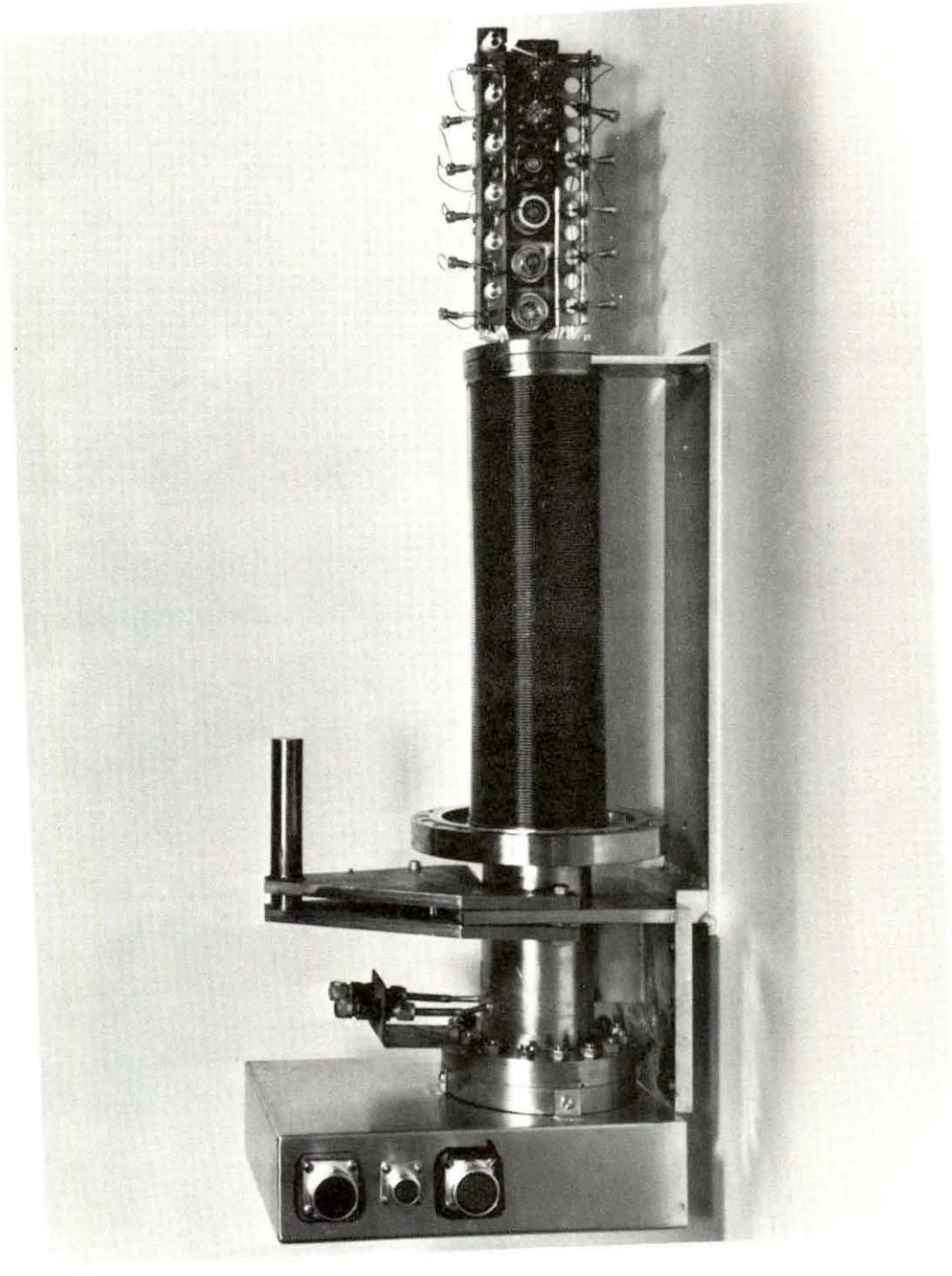

Figure 11: Target assembly for the Van de Graaff accelerator at ORNL in various stages of assembly.

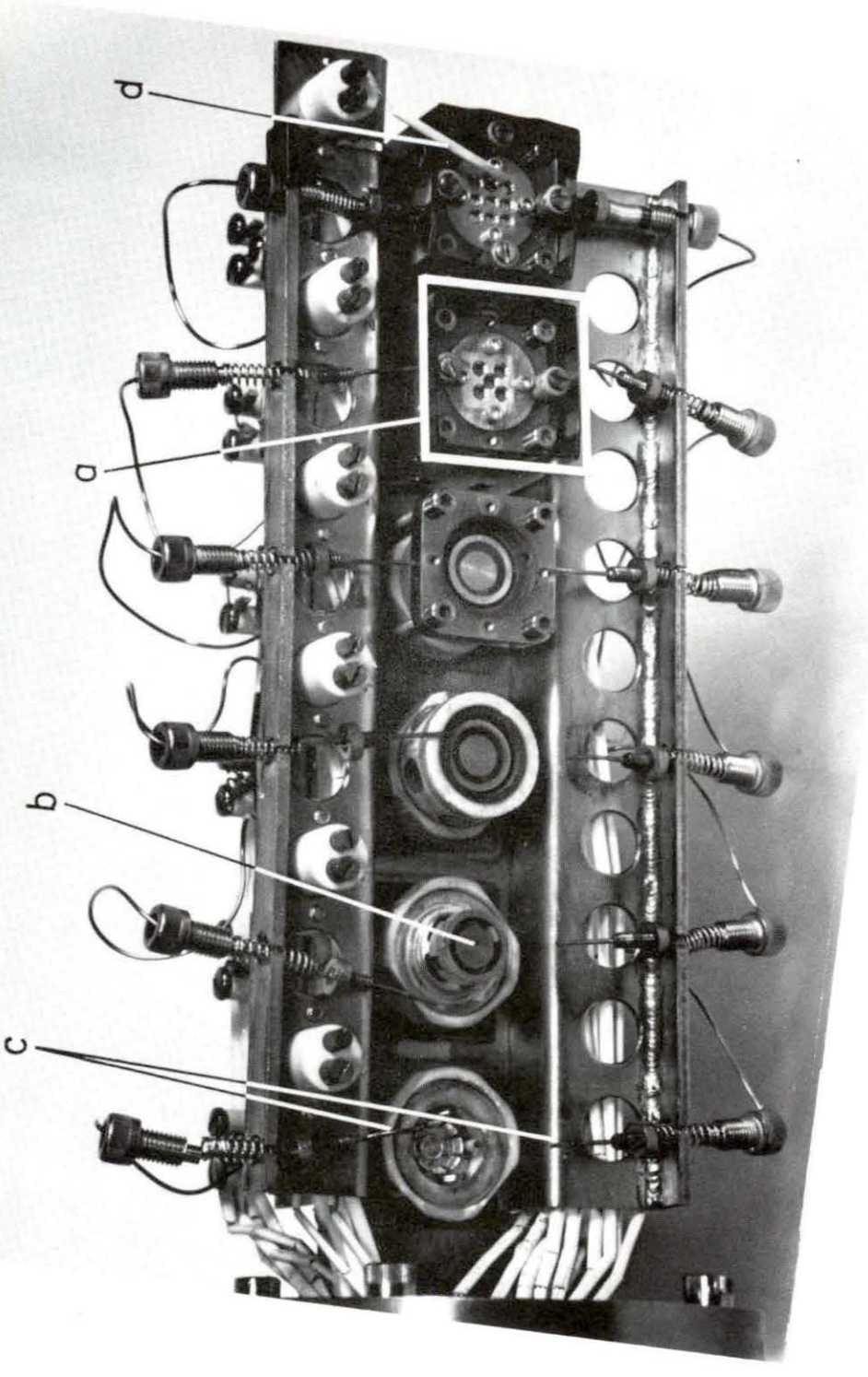
d
a
b
c

while the specimen assembly at ground potential acts as the anode.

Temperature control is gained from signals from either of two 1 mm diameter sheathed Chromel-P-Alumel thermocouples (item C, Figure 11) which are spring loaded into 6 mm deep holes in the edge of each thermalizer block. A third thermocouple output using 0.13 mm diameter Chromel-P-Alumel wires spot welded near the edge of a specimen per target holder-heater (item d, Figure 11) is for monitoring the samples' surface temperatures. The temperature control system responds rapidly to temperature changes and is very stable. The stability and accuracy of temperature output by the system can be maintained to $\pm 1^{\circ}C$ for hours (18).

Ion beam control and diagnostics are achieved by use of the equipment and instrumentation shown in the block diagram of Figure 12. The final ion beam dimensions are established by a pneumatically driven gate valve followed by a 11.0 X 11.0 mm fixed square aperture (18). The ion beam uniformity and intensity are monitored during each "bombardment run" by a nine-hole miniature deep Faraday Cup Array (Figure 13). The deep Faraday cups (DFC's) are positioned in front of the target holder in the beam line every 10 minutes for approximately 20 seconds. The information gathered by the FDC's is sent to an ion beam current integrator which assists in the maintenance of a bombardment run log, listing beam currents and cumulative displacement concentrations for each of the nine targets being bombarded. Once pre-programmed displace-

Figure 14: Loading jig for specimens to be bombarded by ions in the Van de Graaff accelerator at ORNL.

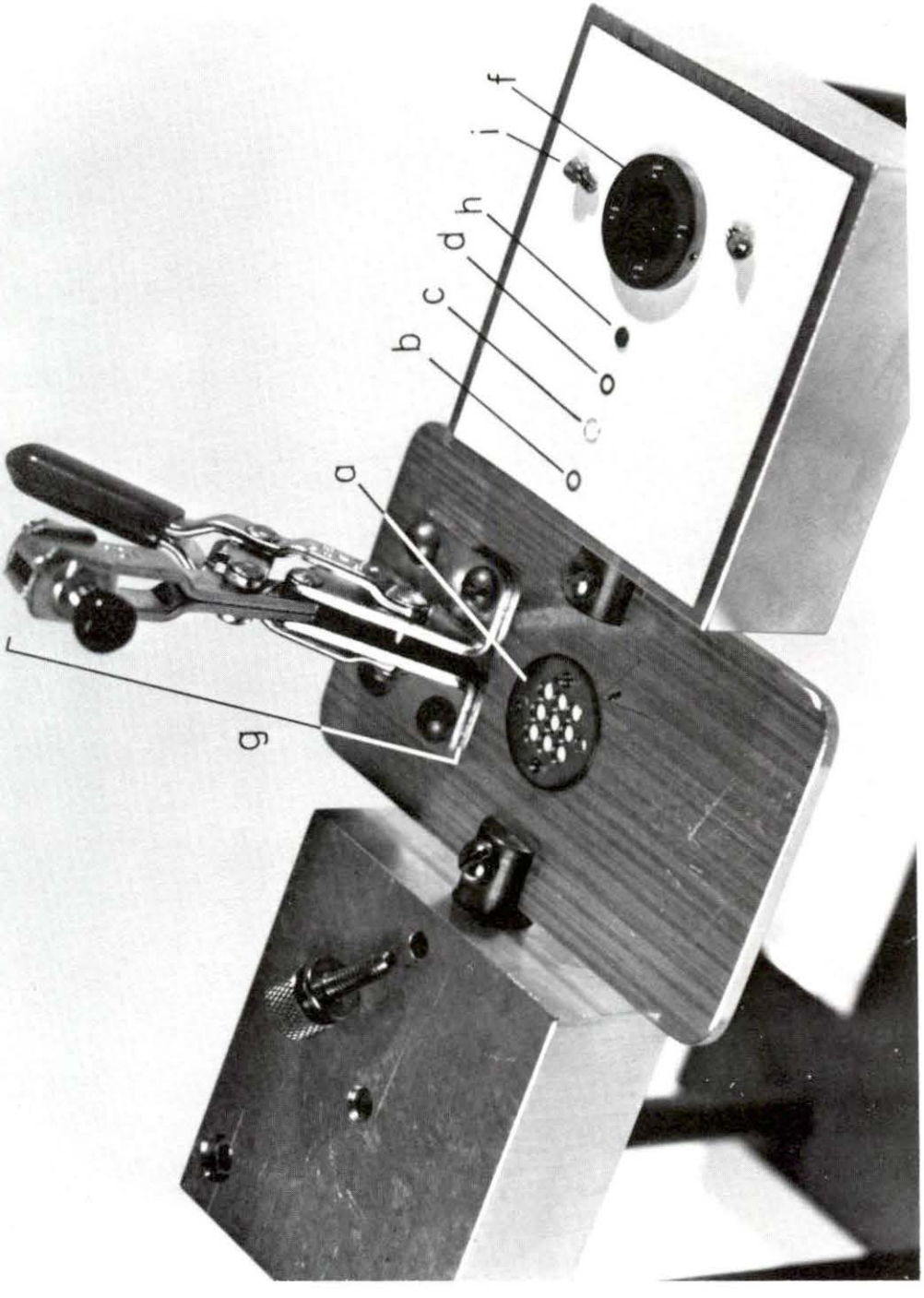
f
i
h
d
c
b
o
o
o
a
g

ment concentration levels are reached, the ion beam is automatically terminated.

Concerning the loading of samples into the target assemblies, Figure 14 shows the loading jig and related components for loading 1/8 inch or 3 mm disc samples into the target holder. First, the face plates (item a) and thermalizer blocks (item f) are ultrasonically cleaned with methyl alcohol. The face plate is placed beam side down in the loading jig. If the 0.001-inch thick molybdenum bar masks (item b) are used to produce a post-bombardment step height between the shielded and unshielded regions, the masks are loaded into the recesses with the bar oriented vertically. The vertical orientation prevents undue shadowing of the light ion beam that impinges upon the target at a 15° angle. Next, a crushable platinum wire ring (item c), usually 0.005 inches thick, is gently pushed into the recess with a rod (not shown) of like diameter. To reduce adherence of the platinum wire to soft samples of materials being irradiated at high temperatures (>600°C), a 0.002-inch-thick stainless steel washer with an oxidized surface finish (item d) is placed on top of the platinum wire. Samples (item h) are now loaded face down into the recesses. The sample to whose face the thermocouple has been welded is loaded in the upper right recess. Next, the thermalizer block (item f) is carefully placed smooth-side down over the samples without dislodging them. Applying the hold down clamp (item g) and rotating the swivel stage upside down, an inspection of the samples is conducted to insure masks are oriented properly, thermocouple leads are properly situated and samples are

securely seated. A clamping force of about 550 N (124 lbs) is applied by a modified toggle-clamp tool to partially compress the platinum wire gasket, eliminating any looseness due to small sample-to-sample variations in thickness. Finally, the four 2-56 socket-head screws (item i) are inserted in the target holder and tightened to maintain the clamp pressure.

The target holders are then placed in the target assembly as shown in Figure 11. Each target holder within the target assembly is designated by a station number 1 through 6 (usually station 1 is to the far right and numbers increase toward the left). Individual samples in each target holder are designated by a matrix position as shown in Figure 15. Accompanying Figure 15 is Table 3 correlating samples to matrix position. This system of identification is needed to aid in post-bombardment sample identification and analysis.

The target assembly (Figure 10) is inserted into the target chamber (item k, Figure 8) and is sealed and evacuated. The chamber can be pumped to a base pressure of 9×10^{-7} Pa (7×10^{-9} torr) while no sample heating is being conducted. While bombarding at elevated temperatures, the pressure normally increases to the low 10^{-5} to high 10^{-6} Pa (low 10^{-7} to high 10^{-8} torr) range (18). The electron guns, samples, target assembly, etc. are normally "conditioned" (out-gased) prior to ion bombardment. Conditioning normally takes from less than 5 min to 30 min depending upon the length of time the electron guns are exposed to air during loading and unloading. After a suitable

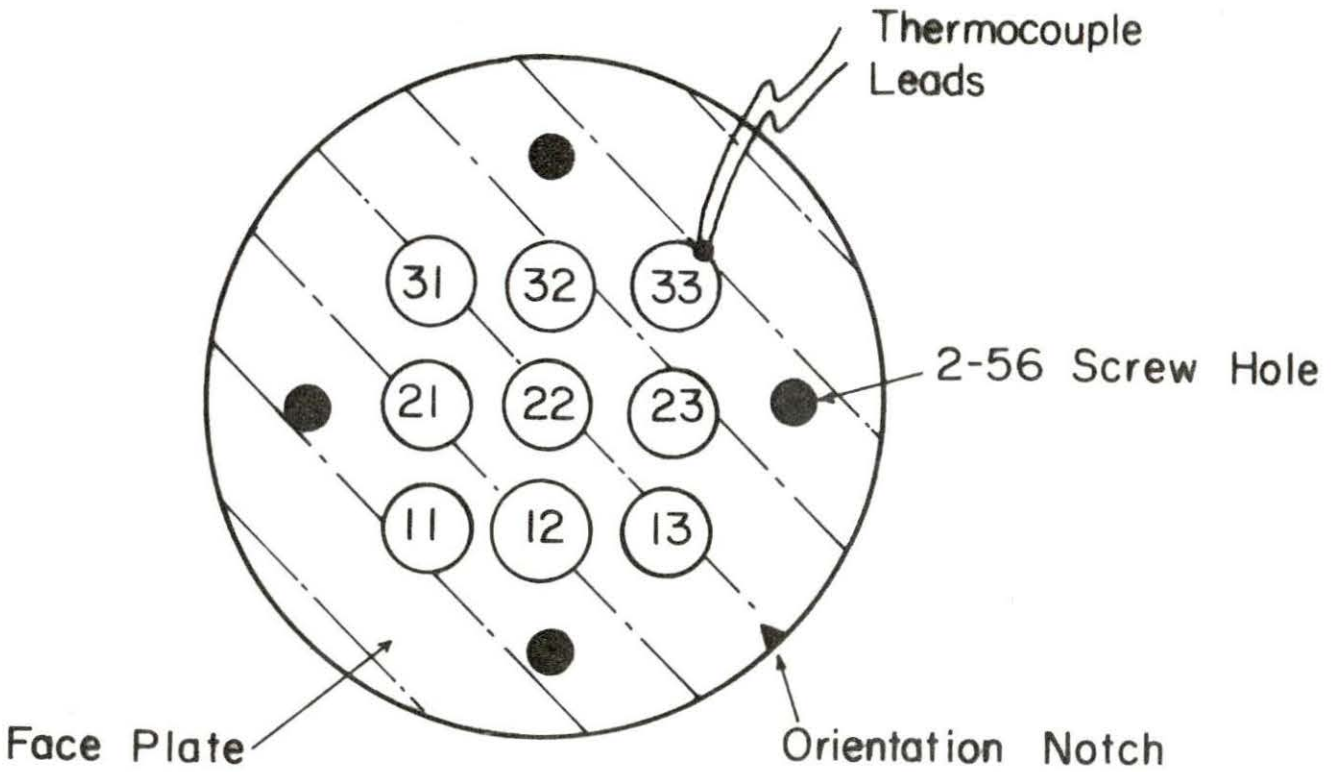

Figure 15: Beam view of target holder and face plate used in ORNL's dual beam Van de Graaff accelerator.

vacuum is obtained and the irradiation temperature is reached, ion bombardment may begin.

Table 3. Matrix positions of AL1 and AL2 doped and undoped samples with respect to positions depicted in Figure 15

Specimen	Matrix Position
AL1	31 and 32
AL1 + 0.1% Y	22 and 23
AL2	11 and 12
AL2 + 0.1% Y	13 and 21
AL1 + 0.3% Y-with thermocouple attached (not used for swelling measurements)	33

AL1 and AL2 undoped and doped samples were irradiated under the following conditions:

Temperature (°C): 500, 577, 653, and 730

Vacuum: 10^{-8} torr

Ions: First sample set bombardment - 4 MeV $^{56}Fe^{2+}$ only

Second sample set bombardment - 4 MeV $^{56}Fe^{2+}$ with simultaneous implantation of 0.4 MeV $^{4}He^{+}$ ions

D. Analysis of Swelling

Procedures as outlined by Gessel (2), in which a profilometer was used to measure step heights, were originally attempted to determine step heights. Gessel observed step heights caused by swelling of about 10^3 Å. Step heights produced in our samples were below 500 Å. Efforts to determine step heights in AL1 and AL2 by profilometry were unsuccessful because of low swelling and rough surface finishes. The rough surface finish in these alloys was due to the second phase (precipitates). An example of the rough surface contour is shown in Figure 16.

Other techniques have been published for determining step heights (23, 24). In the present work, an interferometer was used to make precise determinations of small step heights. The interferometer (the Zeiss Interference Microscope) makes use of a thallium vapor lamp (monochromatic light source of wave length λ = 5400 Å) to establish the interference patterns. The interferometer's 60X magnification makes it possible to recognize minute surface structures and to evaluate them by means of superimposing light interference bands of these features. The depth measuring range of this instrument is about 0.01μ to 2μ. White or monochromatic light can be used.

The phenomenon, which appears when two (or more) light waves are superimposed, is called "interference of light". Only light waves which have the same direction and frequency of vibration can be superimposed. The wave trains emitted by a light source are of finite length; there-

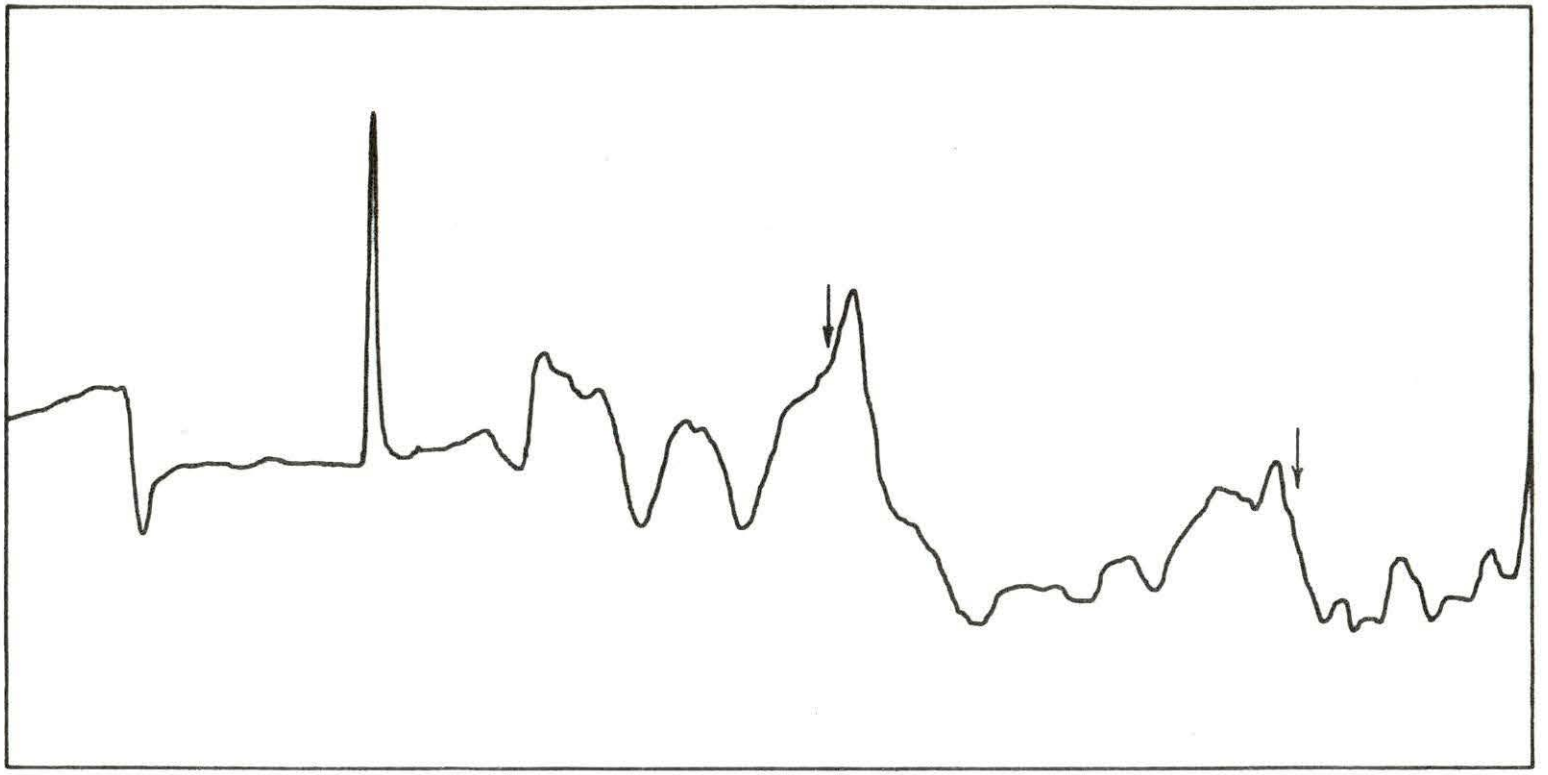

(a) Sloam Dektak trace of post bombarded AL2 (T_I = 570°C) vertical magnification 1 x 10^6 X, horizontal magnification 500X. (Arrows indicate the approximate location of where the step height should be.)

Figure 16: Surface contour of post bombarded AL2 using 4 MeV $^{56}Fe^{2+}$ and 0.4 MeV $^{4}He^{+}$ ions to produce a damage concentration of 100 dpa.

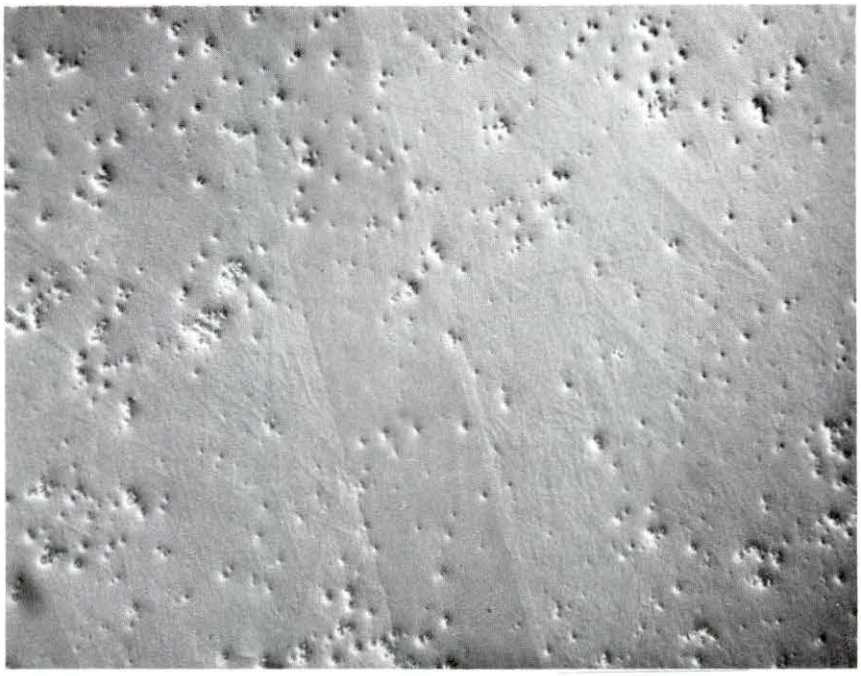

(b) Micrograph of post bombarded AL2 (T_I = 570°C) in which the shielded region produced by the bar mask can easily be seen (50X).

Figure 16: (continued)

fore, one can bring into interference only waves which are from a single light source. If one considers a glass wedge, such as the one in Figure 17, to be illuminated by a monochromatic light source, dark bands are revealed upon examination. At I, a wave train strikes the wedge and is divided into two parts. One part of the light is reflected at the surface and the other part (say point A) penetrates the wedge and is reflected at the basal surface (disregard the part emitted there). In Figure 17b, that portion of the wave containing point A coming from the basal surface has been reflected back and has just reached the upper surface of the wedge. During this time the original wave containing point A' has continued to travel so that A' strikes the upper surface of the wedge; thus, the portions of the waves containing A and A' annul each other and at this point darkness prevails (Figure 17c). At II, wave points B and B' follow the same sequences as those of points A and A'; however, this time the wave segments containing points B and B' fall on wave crests, amplifying each other, and greater brightness prevails. At III, the same conditions exist that were experienced at I and again darkness prevails. It should be noted that the difference in height between I and III is <u>exactly</u> half a wave length of light (Figure 17b). Another attractive feature to this type of instrument is that the wave length of light used (thallium) is finite and constant, eliminating the need for instrument calibrations.

It is instructive at this point to include the optical design of the interferometer for a better understanding of the technique used in analyzing the step heights. Figure 18 shows only the construction

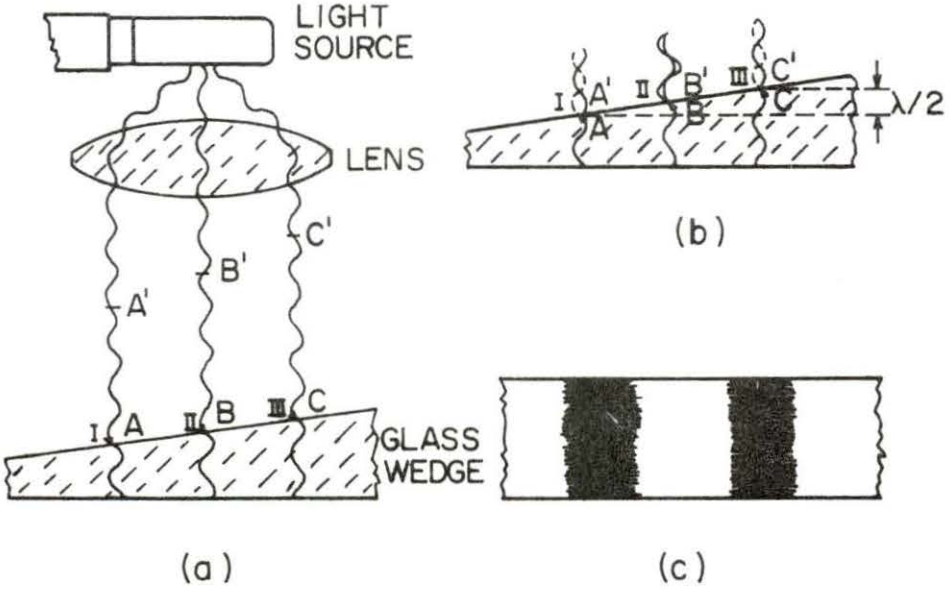

Figure 17: A schematic drawing of the principle of light interference produced in an optical interference microscope (interferometer).

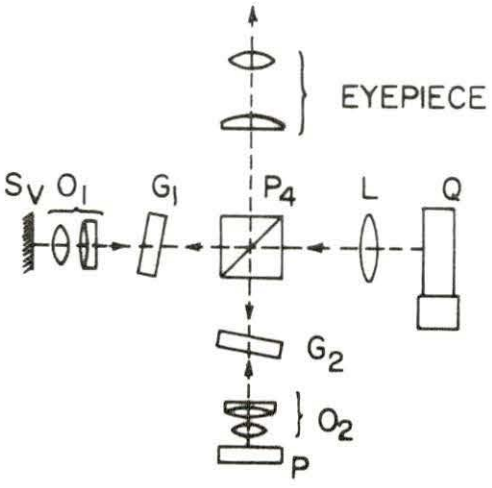

Figure 18: Basic optical design of an optical interference microscope (interferometer).

principle and not the actual optical arrangement. The surface to be examined is illuminated by thallium light (i.e., a monochromatic light source). Proceeding from the light source Q, the light passes via the illumination objective L and to prism P_1 where the beam is divided. One part passes through plane G_2 and objective O_2 to the sample to be examined, P, and is reflected back again to prism P_1. The other part passes through P_1 via G and objective O, to a mirror S_v, and from there, after reflection, back to P_1. In the beam splitting prism P_1 the two beams are superimposed upon each other and are reflected into the eyepiece. The surface of the sample examined appears magnified in the eyepiece while the two beams coming from P and S_v generate interference bands. A interference micrograph of an AL2 sample is shown in Figure 19.

The method of determination of the swelling is illustrated in Figures 20a, 20b, and 20c. Prior to bombardment, a one-mil-thick sheet of molybdenum was placed across a portion of each sample in order to shield a portion of the sample from the iron ion beam or the dual iron and helium beams. Figure 20a shows the interference bands as seen through the interference microscope (interferometer) using a thallium vapor lamp as a light source. Indicated in Figure 20b are the locations of the masked and unmasked regions of the sample. As can be seen from the insert in Figure 20c, the edge of fringe 1 in the masked region (represented by AA) shifts to A'A' in the unmasked region. Similarly, the edge of fringe 2 in the masked and unmasked regions is represented by BB and B'B', respectively. In the insert of Figure 20c, BB is pro-

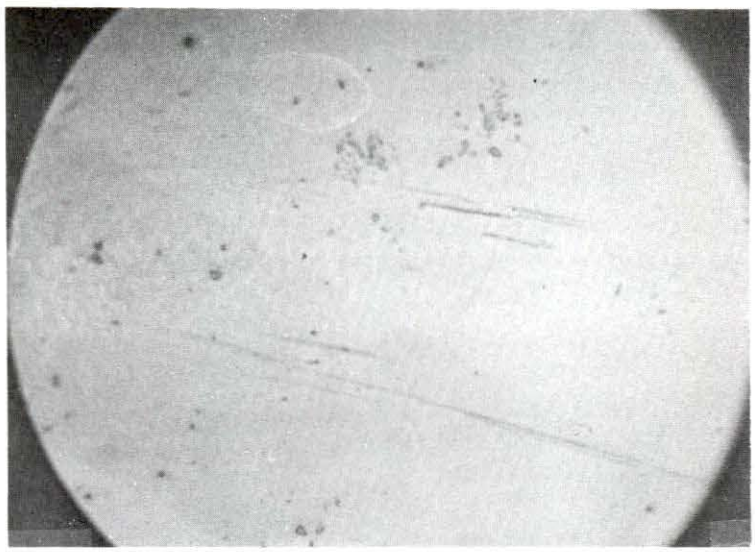

Figure 19A: post bombarded AL2 (Ti = 570°C, 99 DPA) as viewed in an interferometer without superimposed interference bands.

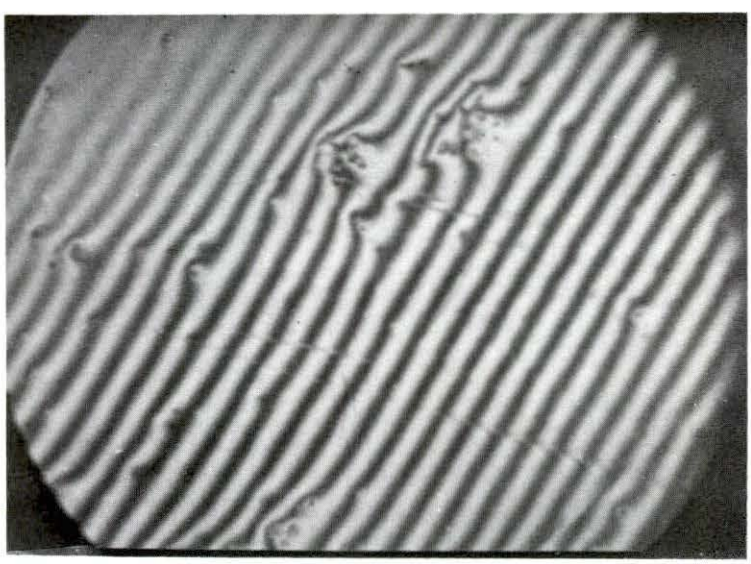

Figure 19B: post bombarded AL2 (Ti = 570°C, 99 DPA) as viewed in an interferometer with superimposed interference bands.

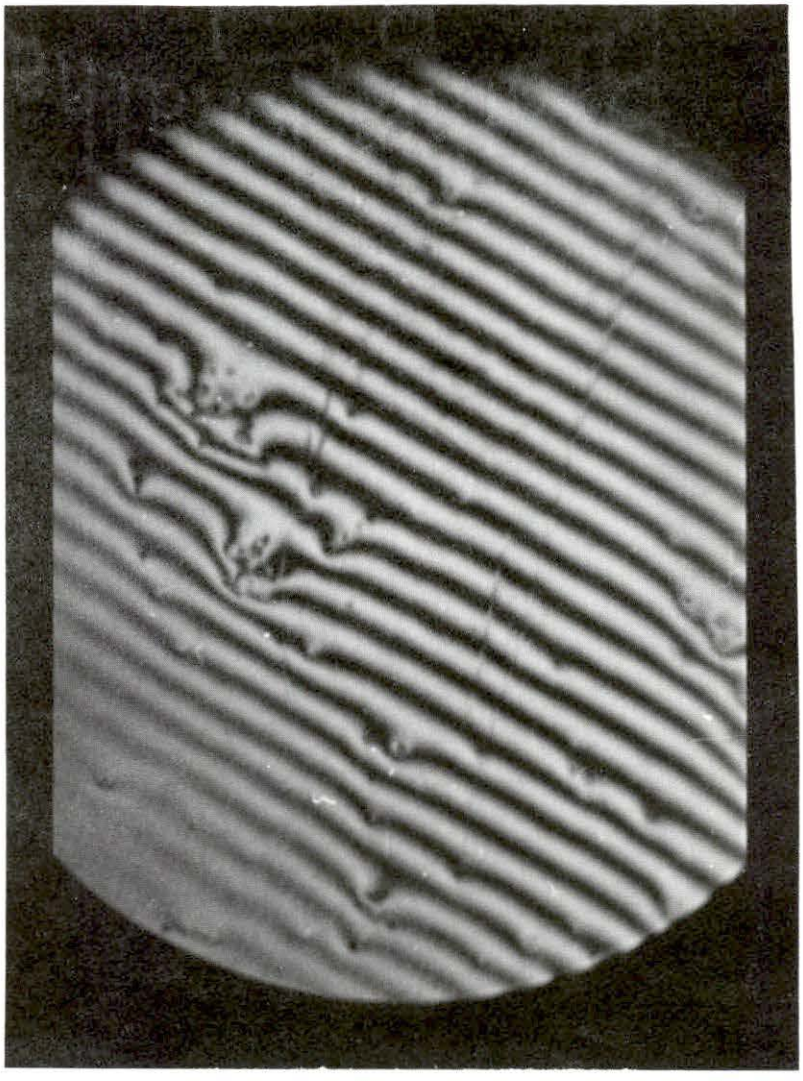

Figure 20A: Interference bands as observed in an interference microscope using a thallium vapor lamps as light source.

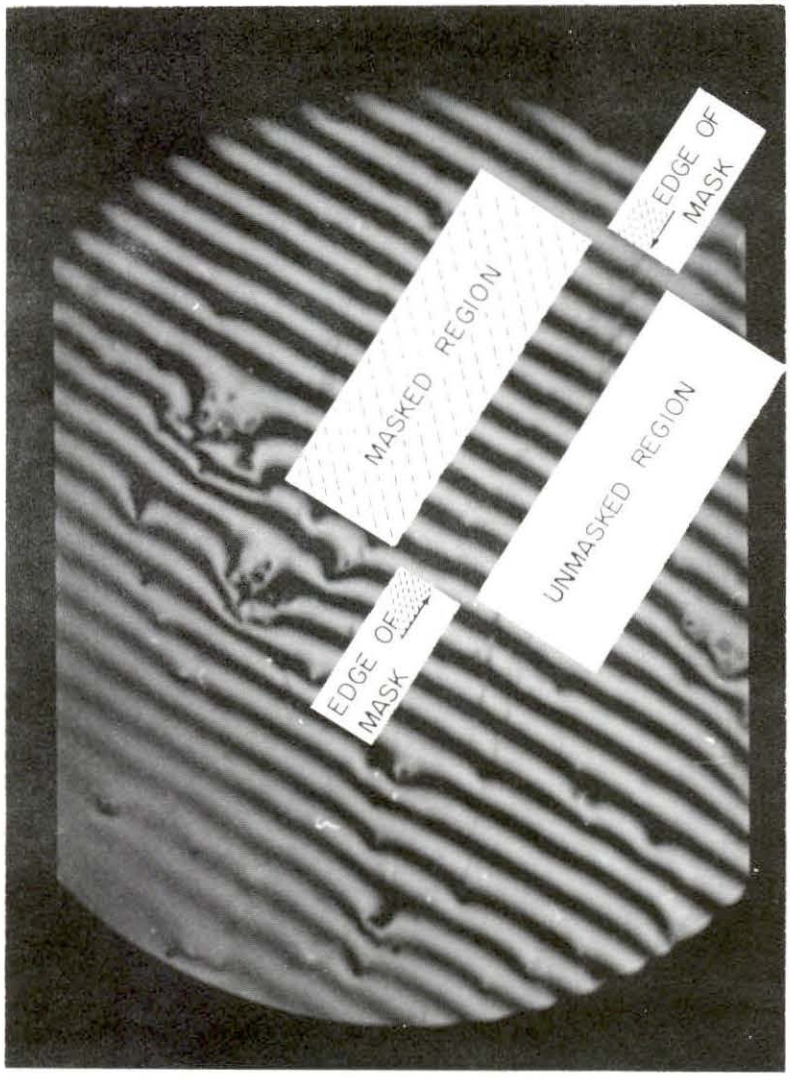

Figure 20B: Same field as shown in Fig. 2A, but identifying the masked and unmasked regions.

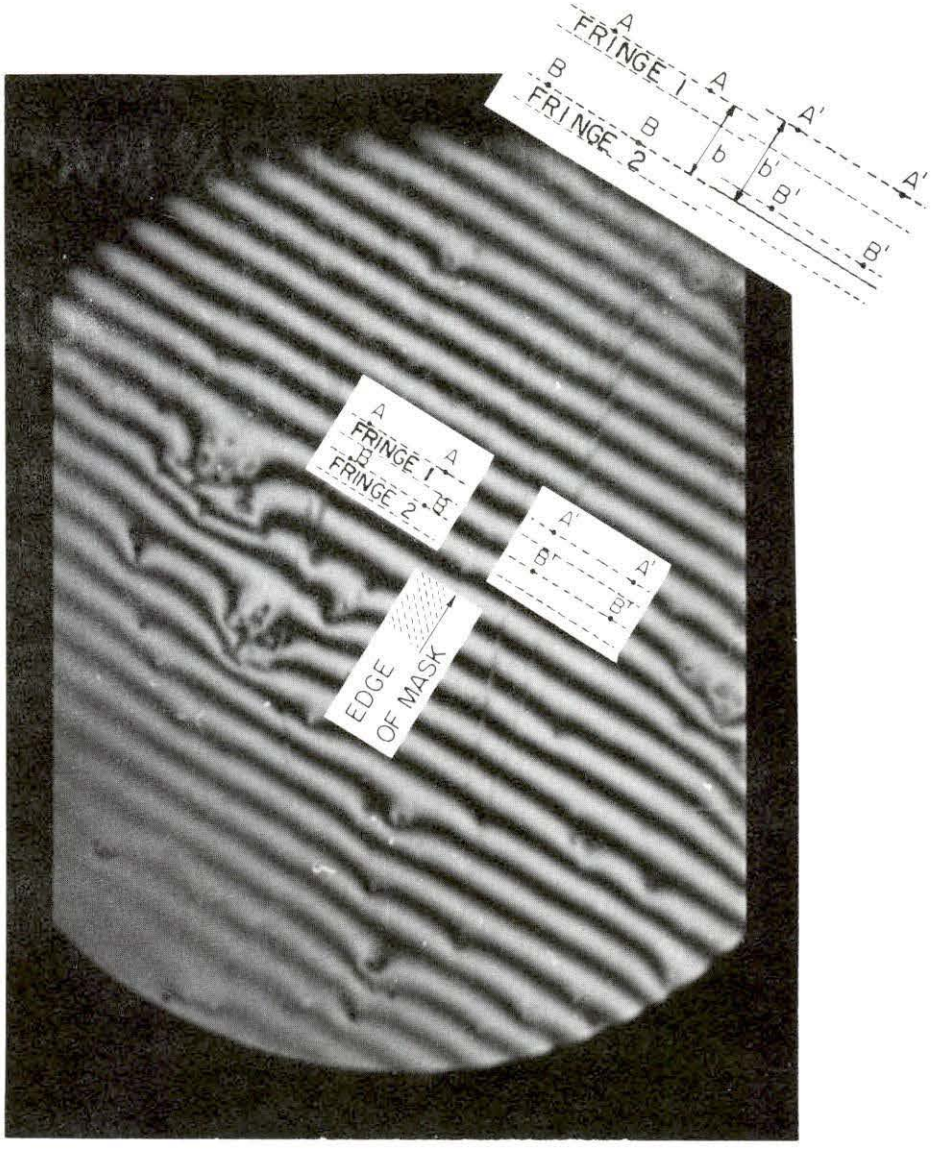

Figure 20C: Same field as shown in Figs. 2A and 2B, illustrating the method of determination of the step height and swelling.

jected from the masked region into the unmasked region and the projection of BB is used as a reference for measuring distances b and b', b being the distance between AA and BB and b' the distance between A'A' and the projected BB. The step height, h, is calculated from the following relationship:

$$h = [(b'-b)/b']\lambda/2$$

where $\lambda/2$ is one-half the wave length of the thallium light source (i.e., 2700 Å). The distances b' and b were measured directly from the photographs, such as shown in Figures 20a, b, and c, to within $\pm$0.005 inches. Approximately 3-5 locations along the masked-unmasked interface were used and the average step height, $\bar{h}$, was calculated. Tables 4 and 5 give the $\bar{h}$ values obtained and also the standard deviations (25)

$$\sigma = [(\frac{1}{N+1}) \sum_{i=1}^{N} (h_i-\bar{h})^2]^{\frac{1}{2}}$$

where h_i refers to an individual determination and N is the number [3-5] of determinations for a given sample. The average standard deviation corresponds to about 15-20 Å.

Swelling is commonly expressed as a relative change in volume, $\frac{\Delta V}{V}$. Percent swelling is calculated from the step height in Å units from the empirical relation, 1% peak swelling = 60 Å step height, as determined by Johnston et al. (9).

Table 4. Irradiation conditions and swelling results for AL1 and AL2 without and with 0.1% Y, bombarded with 4 MeV $^{56}Fe^{2+}$ ions only

Sample	Irradiation Temp (C°)	Displacement Concentration (dpa)	He Implanted (appm)	Average Step Height (Å)	Standard Deviation (Å)	Swelling (%)
AL1	505	108	0	-[a]		-
"	572	106	"	147	12	2.5
"	656	115	"	79	26	1.3
"	716	118	"	40	24	0.6
AL1+0.1% Y	581	108	"	-		-
"	605	133	"	111	26	1.8
"	653	128	"	83	15	1.4
"	723	131	"	-		-
AL2	513	95	"	-		-
"	577	89	"	231	9	3.9
"	649	91	"	123	12	2.1
"	723	88	"	-		-
AL2+0.1% Y	509	103	"	-		-
"	567	95	"	187	20	3.1
"	646	93	"	67	11	1.1
"	749	98	"	54	3	0.9

[a]Not detectable.

Table 5. Irradiation conditions and swelling results for AL1 and AL2 without and with 0.1% Y, bombarded simultaneously with 4 MeV $^{56}Fe^{2+}$ and 0.4 MeV $^{4}He^{+}$ ions

Sample	Irradiation Temp (C°)	Displacement Concentration (dpa)	He Implanted (appm)	Average Step Height (Å)	Standard Deviation (Å)	Swelling (%)
AL1	499	110	65	125	10	2.1
"	576	111	68	343	8	5.7
"	651	124	66	187	11	3.1
"	728	121	65	136	13	2.3
AL1+0.1% Y	552	123	65	183	33	3.1
"	607	128	68	248	29	4.7
"	664	118	66	188	16	3.1
"	743	139	65	161	30	2.7
AL2	502	83	65	112	18	1.9
"	570	99	68	466	20	7.7
"	643	76	66	169	20	2.8
"	725	79	65	83	27	1.4
AL2+0.1% Y	507	105	65	121	5	2.0
"	582	117	68	246	16	4.1
"	634	97	66	219	33	3.7
"	728	107	65	155	29	2.6

IV. RESULTS

Post-bombardment analyses were conducted on AL1 and AL2 undoped and doped (0.1% Y) samples. Irradiation conditions and swelling results for these bombardments are listed in Tables 4 and 5.

For heavy-ion (i.e., 4 MeV $^{56}Fe^{2+}$ ions, Figure 21) bombardment only, the peak swelling (at 572°C) in undoped AL1 was 2.5%, whereas the peak swelling (at 605°C) in yttrium-doped AL1 was 1.8%. Thus, the addition of 0.1% Y caused a 28% decrease in the peak swelling in AL1. Furthermore, Figure 21 shows the peak swelling (at 577°C) for undoped AL2 to be 3.9%, whereas the peak swelling (at 567°C) for yttrium-doped AL2 was 3.1%. Thus, the addition of 0.1% Y produced a decrease of about 20% in the peak swelling for AL1.

For 4 MeV $^{56}Fe^{2+}$ ion bombardments with the coimplantation of helium by a 0.4 MeV $^{4}He^{+}$ ion beam (Figure 22), it was observed that the peak swelling was 5.7% and 4.7% (at 576°C and 607°C, respectively) for undoped and yttrium-doped AL1, respectively, giving rise to about a 17% decrease in swelling due to the 0.1% Y addition. Likewise, the yttrium addition to AL2 decreased peak swelling from 7.7% (at 570°C) in the undoped sample to 4.1% (at 582°C) in the doped sample, which amounts to a decrease of about 47% in the peak swelling for AL2.

The effects of simultaneously implanting helium during heavy-ion bombardment are illustrated in Figures 23 and 24. The coimplantation of helium in AL1 (Figure 23) increased the peak swelling from 2.5% to 5.7% and from 1.8% to 4.7% in undoped and doped samples, respectively.

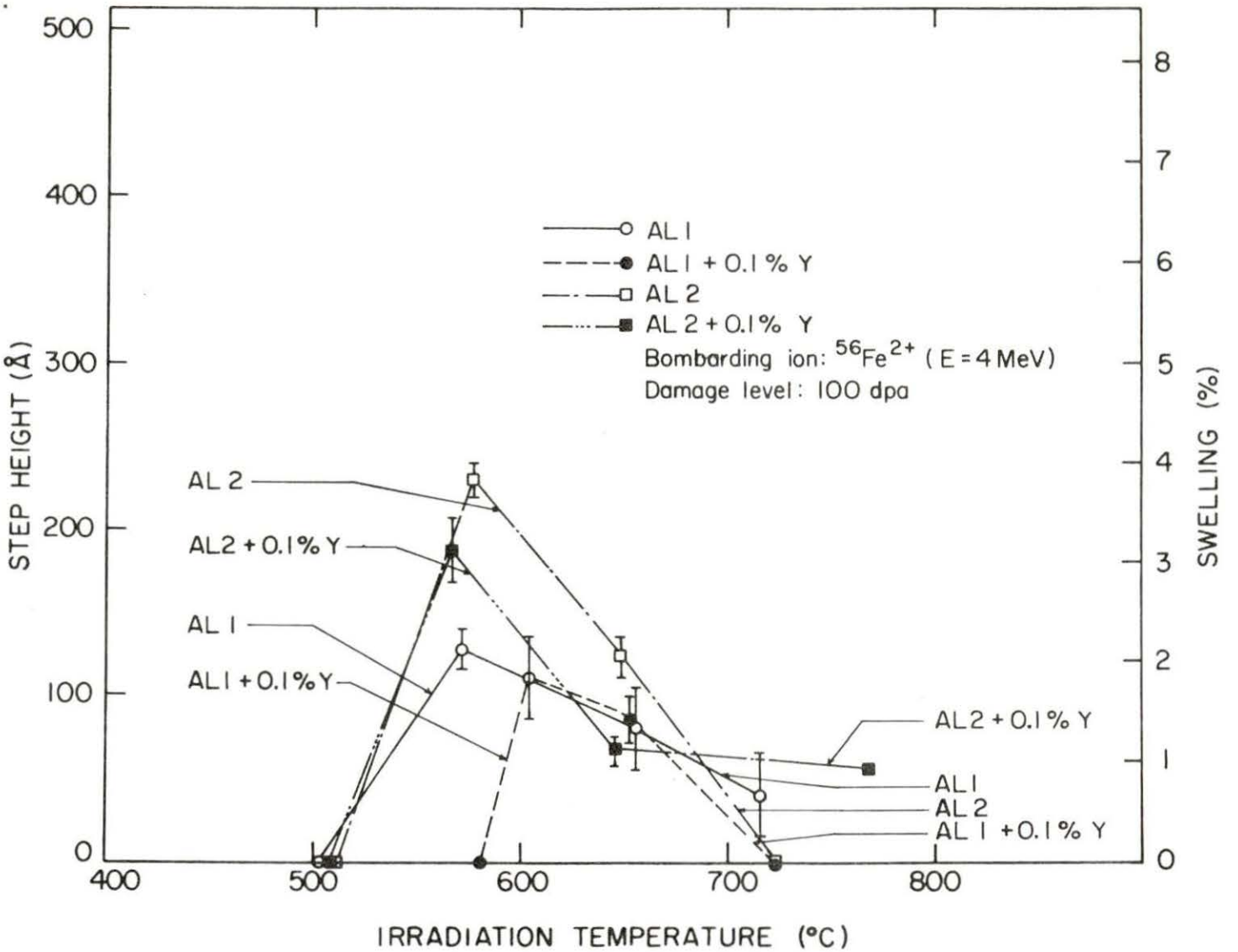

Figure 21: Step height and swelling versus irradiation temperature for D21 and D68 without and with 0.1% yttrium, bombarded with 4 MeV $^{56}F^{2+}$ ions only.

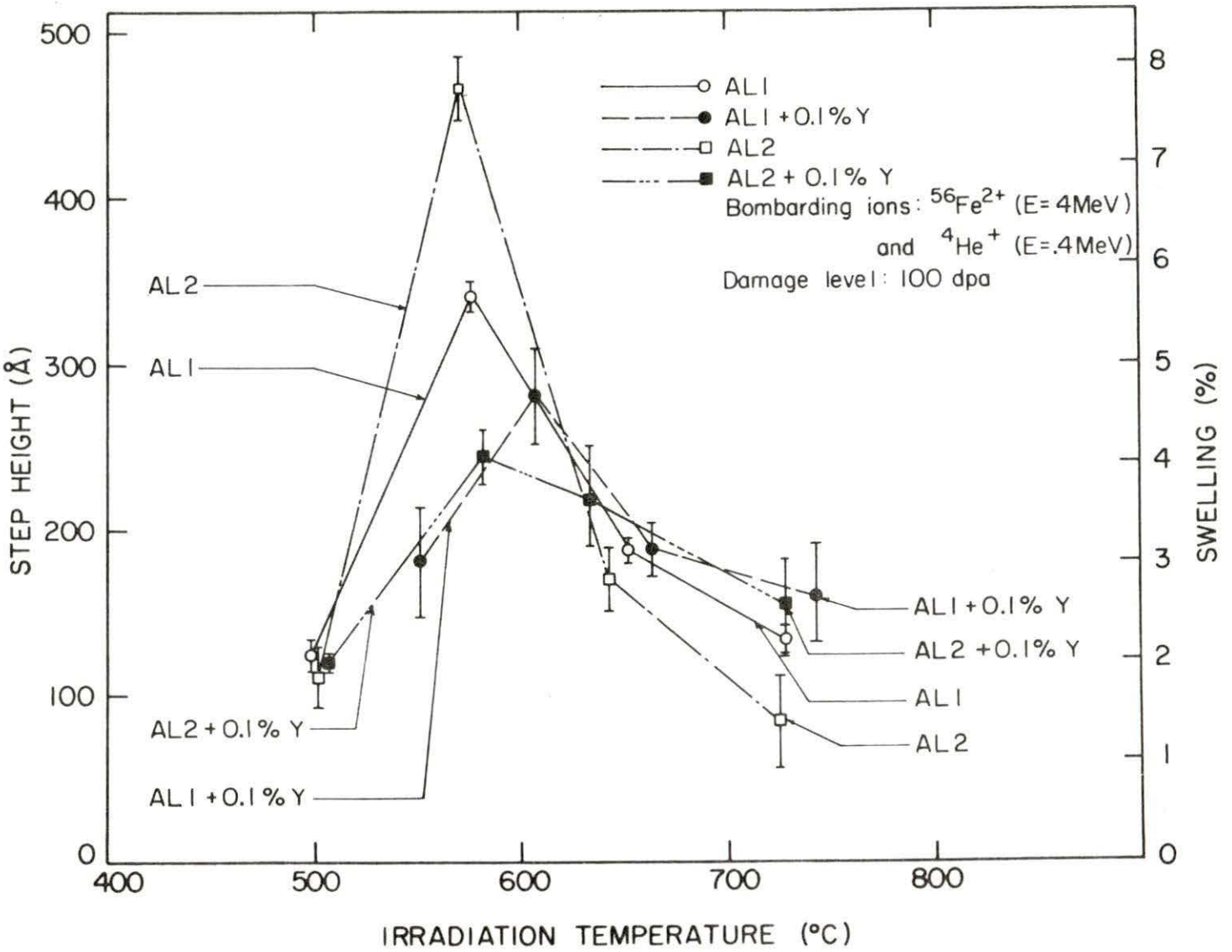

Figure 22: Step height and swelling versus irradiation temperature for D21 and D68 without and with 0.1% yttrium, bombarded with 4 MeV $^{56}Fe^{2+}$ and 0.4 MeV $^{4}He^{+}$ ions.

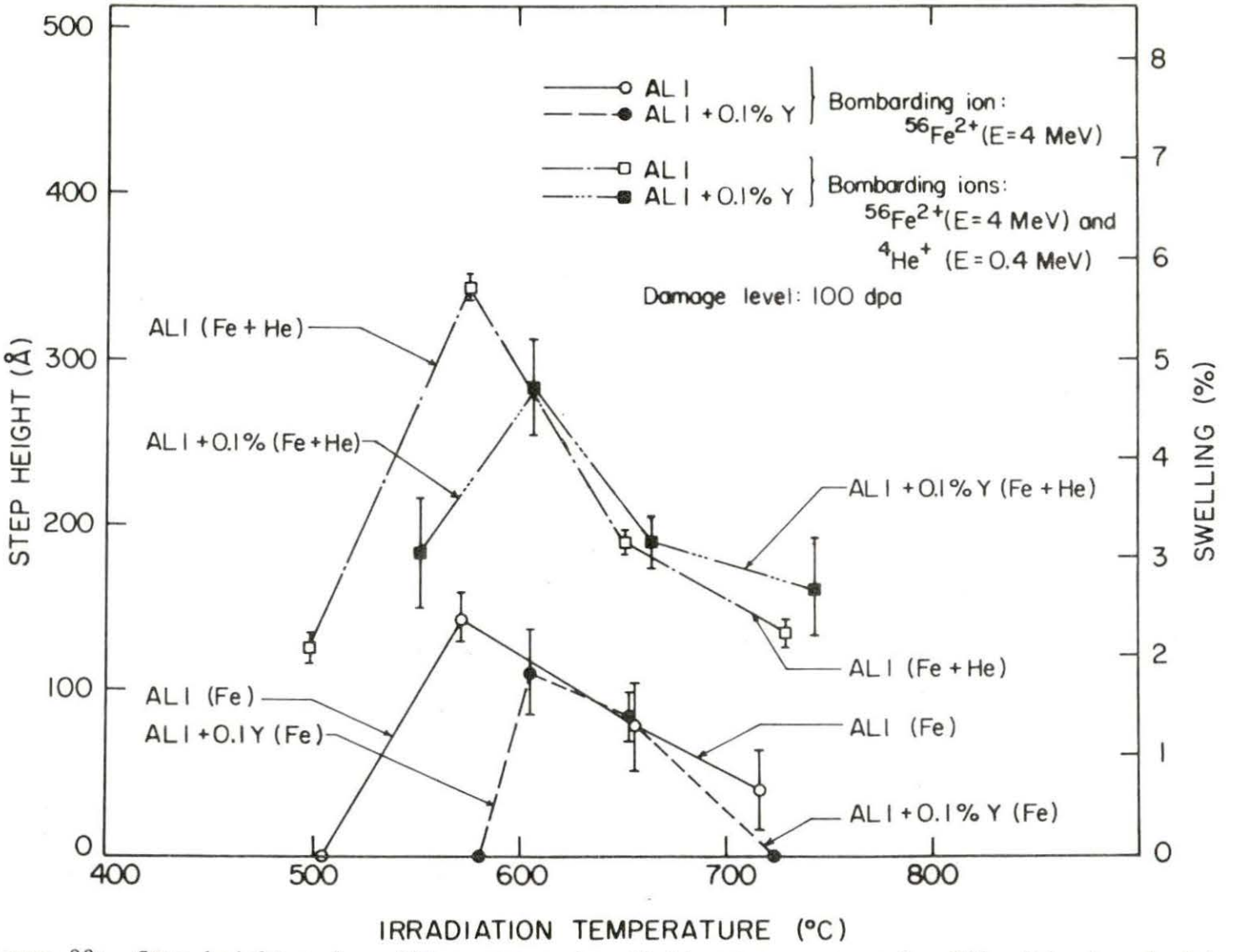

Figure 23: Step height and swelling versus irradiation temperature for D21 without and with 0.1% yttrium, bombarded by 4 MeV $^{56}Fe^{2+}$ ions without and with the coimplantation of 0.4 MeV $^{4}He^{+}$ ions.

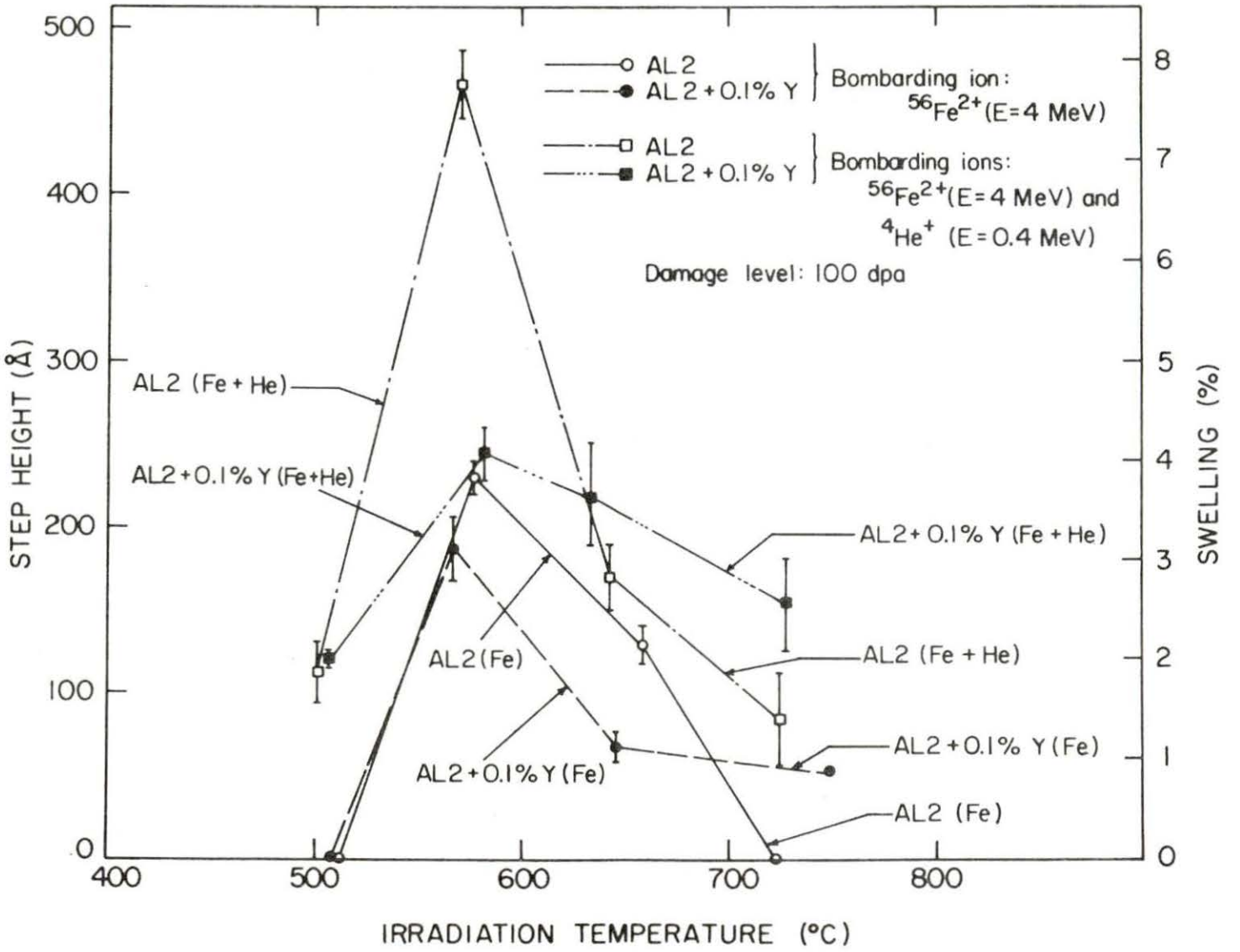

Figure 24: Step height and swelling versus irradiation temperature for D68 without and with 0.1% yttrium, bombarded by 4 MeV $^{56}Fe^{2+}$ ions without and with the coimplantation of 0.4 MeV $^{4}He^{+}$ ions.

Thus, coimplanted helium increased the peak swelling by factors of 2.3 and 2.6 in the undoped and doped samples, respectively. As for AL2, Figure 24 shows that coimplantation of helium resulted in peak swelling increases from 3.9% to 7.7% in the undoped samples and from 3.1% to 4.1% in the doped samples. One can conclude from this that coimplanted helium increased swelling in AL2 by factors of 2.0 and 1.3 for undoped and doped samples, respectively.

It should be noted that in all cases where similar sample comparisons are made (i.e., undoped with undoped and doped with doped) and where bombardment conditions were similar (i.e., single with single beam and dual with dual beam), AL1 showed less peak swelling than did AL2. It is difficult to draw conclusions concerning shifts in peak swelling temperatures due to helium implantations or yttrium additions. It is also interesting to note that samples exhibiting the greatest peak swelling do not necessarily exhibit greater swelling than other samples at other temperatures. One example of this can be seen in Figure 22. AL2 swelled the greatest at peak swelling temperatures, while at all other temperatures it swelled the least.

V. DISCUSSION

The addition of 0.1% yttrium decreased peak swelling in AL1 and AL2. It is postulated that yttrium, acting as an oversized substitutional impurity, traps vacancies, thus increasing the likelihood of a mobile interstitial finding and recombining with the vacancy, which ultimately decreases void swelling. The trapping of vacancies instead of interstitials by yttrium appears reasonable because a vacancy-solute atom complex has a lower energy than an isolated vacancy and isolated solute atom, when the solute atom is oversized. Also, it is widely observed that void formation is enhanced when gas atoms are present (26-29), and Farrell (26) states that substitutional impurities lessen this effect of gas atoms by decreasing the critical fluence for void formation. Three reasons for the effect of substitutional solutes given by Farrell (26) are:

1. Solute trapping of point defects increases the probability of interstitial-vacancy recombination.
2. Solute atoms segregate at sinks for point defects, reducing the sink capture efficiencies.
3. The interstitial-vacancy separation distance in displacement cascades is reduced when solute atoms are present.

Another possible effect of the yttrium addition could be the formation of a second phase, which segregates into stringers parallel to the rolling direction. This is illustrated in Figure 25 and 26, which show an increased amount of stringers in AL1 and AL2 with increasing

Figure 25: Micrographs of AL1 showing the increase in the formation of second phase stringers parallel to the rolling direction with increases in yttrium content.

(a) AL1 undoped (100X)

(b) AL1 doped with 0.1% yttrium (100X)

(c) AL1 doped with 0.3% yttrium (100X)

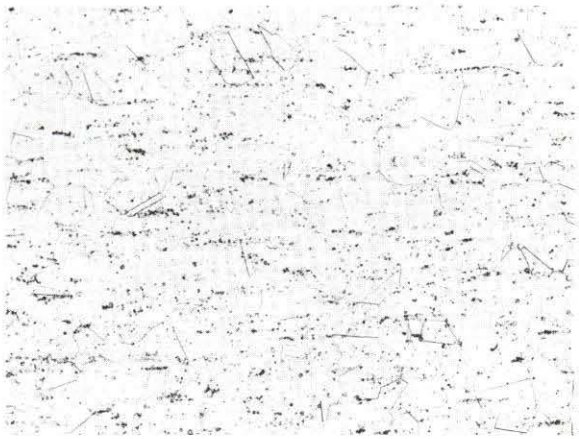

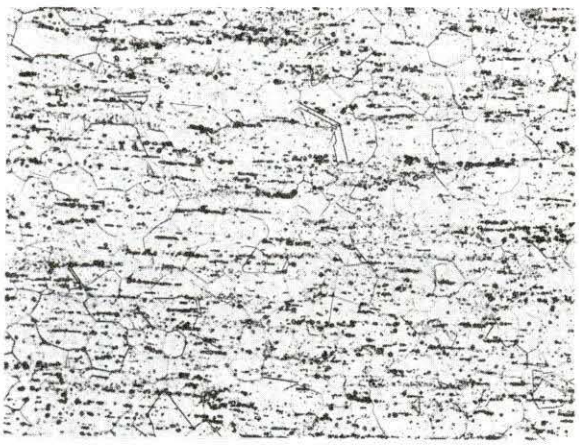

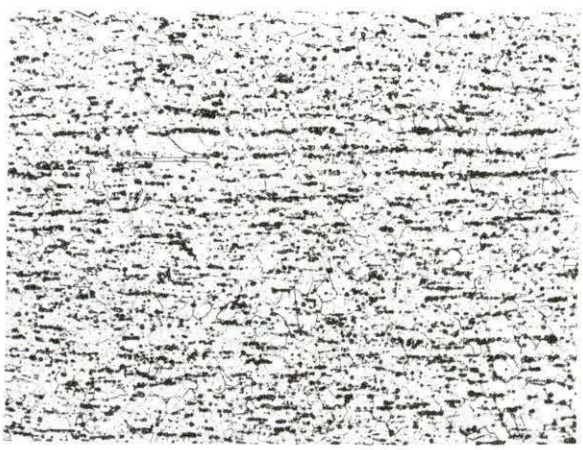

Figure 26: Micrographs of AL2 showing the increase in the formation of the second phase stringers parallel to the rolling direction with increases in yttrium content.

(a) AL2 undoped (100X)

(b) AL2 doped with 0.1 % yttrium (100X)

(c) AL2 doped with 0.3 % yttrium (100X)

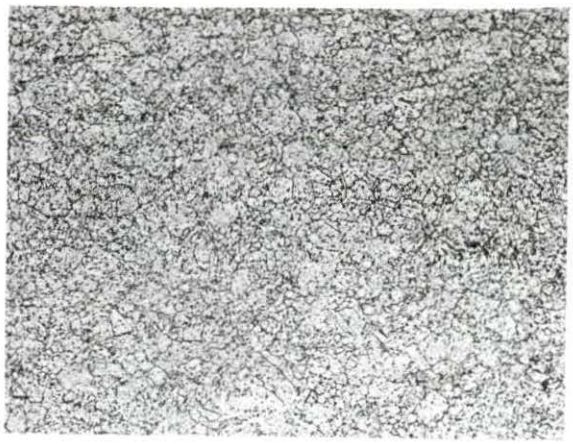

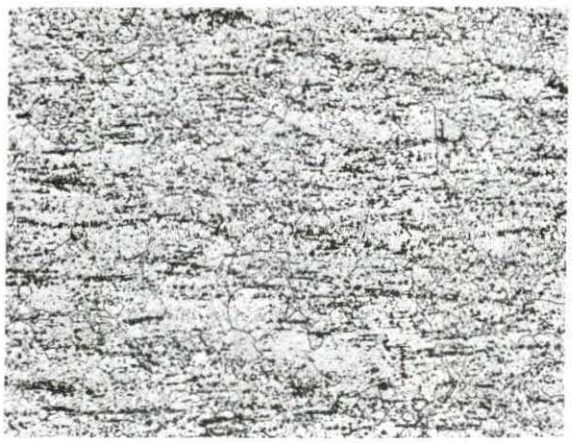

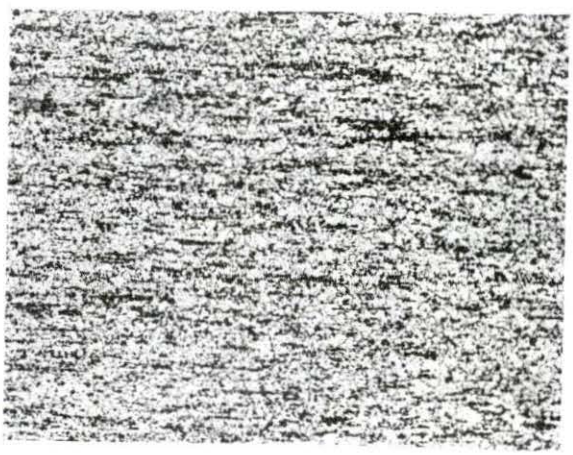

yttrium content. Roberts et al. (30) observed such stringers in an Fe-15% Ni-4% Al alloy doped with 0.86% Y. The stringers had the composition YFe_9. Likewise, the studies of Francis (6) on a niobium stabilized Fe-20% Cr-25% Ni steel doped with 0.7% Y resulted in an yttrium distribution in the steel consisting of second phase particles [$Y(Ni,Fe)_9$ and YNi_5] within an austenitic matrix.

Studies on Fe-Ni-Cr alloys have indicated:

1. The higher the Ti/Al ratio, the greater the resistance of the alloy to swelling (31).
2. For Ni ion bombardments, the swelling decreases with increasing Ni concentration up to 40-45% (3).

Based on the above, one would have expected AL2 to have swelled less than AL1; however, this was not observed. The peak swelling for AL1 was lower than that for AL2 in the present study.

Generally, the less pure an alloy is, the greater is its resistance to irradiation damage. Not all metals exhibit radiation-induced void swelling. The nucleation of voids can be combated by increasing the recombination of interstitial-vacancy pairs or by storing excess vacancies in dislocation loops (26). Zr and Ti are two outstanding examples of metals that have not exhibited void swelling for the highest fluences employed. AL1 contains higher concentrations of these two elements than does AL2. Ti and Si retard cavitation and dislocation loop evolution, reducing vacancy aggregation into voids and absorption of excess interstitials into dislocation loops, thus promoting interstitial-vacancy recombination.

The coimplantation of 0.4 MeV $^{4}He^{+}$ ions increased the peak swelling for both undoped and doped AL1 and AL2. Cavity nucleation and the formation of dislocation structures are drastically enhanced by the inert gas He (26). On an atom-for-atom basis, He is a stronger promoter of cavity nucleation than is H, O, or N.

While this thesis deals with the coimplantation of He, the method by which He is injected drastically affects swelling results (26-29). Cavity nucleation is overstimulated and there is a different temperature response of swelling when He is preimplanted (26).

Hall (27) suggests that dislocation loops are formed by interstitial clusters while vacancies and He form cavities. The presence of He stabilizes vacancy clusters and affects cavity nucleation in three ways. First, a sufficient number of vacancy - He pairs form early during irradiation, and cavity formation shifts to lower fluences than would have occurred in the absence of the inert gas. Secondly, coimplanted He raises the upper temperature for swelling by prolonging survival of vacancies (26). Finally, cavity number densities increase with increasing gas production rates at fixed times (27).

The presence of He will modify dislocation structure evolution, if present in sufficient quantities during loop nucleation periods (29). Interstitial clusters form dislocation loops which preferentially absorb interstitials, leaving excess vacancies, thus increasing void swelling. Collision cascades collapse into loops annihilating some vacancies prior to the loop being consumed by interstitials (29). Surviving vacancies are then free to migrate and coalesce at gas clusters.

VI. SUMMARY

Candidate Liquid Metal Fast Breeder Reactor cladding alloys AL1 (Fe-26% Ni-9% Cr) and AL2 (Fe-35% Ni-12% Cr) without and with the addition of 0.1% yttrium were bombarded by 4 MeV $^{56}Fe^{2+}$ ions without and with simultaneous bombardment by 0.4 MeV $^{4}He^{+}$ ions. These bombardments were conducted at various irradiation temperatures to determine the effect of yttrium on void swelling. The addition of yttrium decreased peak swelling for 4 MeV $^{56}Fe^{2+}$ ion bombarded AL1 and AL2 by 28% and 20%, respectively. In all cases where similar sample comparisons were made (i.e., undoped with undoped and doped with doped) and where bombardment conditions were similar (i.e., single with single beam and dual with dual beam), AL1 showed less peak swelling than did AL2. Simultaneously implanting helium during heavy-ion bombardment increased peak swelling in undoped and doped AL1 by factors of 2.3 and 2.6, respectively. It was also observed that the coimplantation of helium in undoped and doped AL2 increased peak swelling by factors of 2.0 and 1.3, respectively. No conclusions were drawn with respect to shifts in peak swelling temperatures due to yttrium additions or helium implantations.

VII. BIBLIOGRAPHY

1. J. J. Duderstadt and L. J. Hamilton, Nuclear Reactor Analysis (John Wiley & Sons Inc., New York, N.Y., 1976).

2. G. R. Gessel, "Effects of Minor Alloying Additions on the Strength and Swelling Behavior of an Austenitic Stainless Steel", Oak Ridge National Laboratory, ORNL/TM-6359 (June 1978).

3. W. G. Johnston, J. H. Rosolowski and A. M. Turkalo, "An Experimental Survey of Swelling in Commercial Fe-Cr-Ni Alloys Bombarded with 5 MeV Ni Ions", J. Nucl. Matls. 54, 24 (1974).

4. A. F. Rowcliffe, E. H. Lee, and P. S. Sklad, "The Effects of Phase Instabilities on the Correlation of Nickel Ion and Neutron Irradiation Swelling in Solution Annealed 316 Stainless Steel", International Conference on Irradiation Behavior of Metallic Materials for Fast Reactor Core Components, Ajaccio, Corsica (June 1979).

5. J. W. Bennett and K. E. Horton, "Materials Requirements for Liquid Metal Fast Breeder Reactors", Met. Trans. 9A, 143 (1978).

6. J. M. Francis, "Optimization of the Composition of 20% Cr/25% Ni/Nb Steels for a Civil AGR System on the Basis of Oxidation Resistance", J. Br. Nucl. Energy Soc. 8, 333 (1969).

7. M. W. Wright et al., "Preparation, Melting and Properties of Gadolinium and Europium Alloys", Second United Nations Conf. on the Peaceful Uses of Atomic Energy, 5, 390 (1958).

8. P. C. S. Wu (Ward), "Reactions of Europia with Austenitic Stainless Steels", Trans. Am. Nucl. Soc. 21, 184 (1975).

9. W. G. Johnston, T. Lauritzen, J. H. Rosolowski, and A. M. Turkalo, "The Effects of Metallurgical Variables on Void Swelling", in Radiation Damage in Metals, edited by N. L. Peterson and S. D. Harkness (American Society for Metals, Metals Park, OH, 1976) p. 227.

10. C. Cawthorne and E. J. Fulton, "Voids in Irradiated Stainless Steel", Nature 216, 575 (1966).

11. S. H. Bush, "Mechanisms of Irradiation Damage in Irradiation Effects in Cladding and Structural Materials", Am. Soc. Metals 11, 11 (1965).

12. L. K. Mansur and M. H. Yoo, "Advances in the Theory of Swelling in Irradiated Metals and Alloys", J. Nucl. Matls. 86, 523 (1979).

13. H. Wiedersich, "Theory of Defect Clustering and Void Formation", in Radiation Damage in Metals edited by N. L. Peterson and S. D. Harkness (American Society for Metals, Metals Park, OH, 1976) p. 227.

14. P. R. Huebotter and T. R. Bump, "Implications of Metal Swelling in Fast Reactor Design", in Radiation-Induced Voids in Metals, AEC Symposium Series 26, 84 (1971).

15. A. C. Damask and G. J. Dienes, Point Defects in Metals (Gordon and Breach, New York, 1963).

16. D. R. Olander, Fundamental Aspects of Nuclear Reactor Fuel Elements (Technical Information Center, Energy Research and Development Administration, Oak Ridge, Tenn. 1976).

17. M. B. Lewis, N. H. Packan, G. F. Wells and R. Buhl, "Improved Techniques for Heavy-Ion Simulation of Neutron Radiation Damage" in Nuclear Instruments and Methods, 167, 233 (1979).

18. N. H. Packan and R. A. Buhl, "A Multispecimen Dual-Beam Damage Chamber", Oak Ridge National Laboratory, ORNL/TM-7276 (June, 1980).

19. L. K. Mansur, "Void Swelling in Metals and Alloys under Irradiation", Am. Nucl. Soc. Crit Rev. 40, 5 (Aug. 1978).

20. T. A. Gabriel, B. L. Bishop and F. W. Wiffen, "Calculated Irradiation Response of Materials Using Fission Reactor (HFIR, ORR, and EBR-11) Neutron Spectra", Oak Ridge National Lab, ORNL/TM-6361 (Aug. 1979).

21. E. H. Lee and A. F. Rowcliffe, "Multiple Sectioning and Perforation Techniques for TEM Sub-Surface Studies", Microstructural Science 7, 403 (1979).

22. L. K. Mansur, "Effects of Point Defect Trapping and Solute Segregation on Irradiation-Induced Swelling and Creep", J. Nucl. Matls., 83, (1979).

23. A. Boyde and P. G. T. Howell, "Taking, Presenting and Treating Stereo Data from the SEM II", Scanning Electron Microscopy, 1, 571 (1977).

24. P. G. T. Howell, "Taking, Presenting and Treating Stereo Data from the SEM", Scanning Electron Microscopy, 1, 679, (1975).

25. P. V. Bevington, Data Reduction and Error Analysis for the Physical Sciences, (McGraw-Hill Inc., New York, 1969).

26. K. Farrell, "Experimental Observations of Effects of Inert Gas on Cavity Formation During Irradiation", presented at Consultant Symposium on Rare Gases in Metals and Ionic Solids, Harwell England, Sept. 10-14, 1979. To be published in proceedings.

27. B. O. Hall, "Effects of Simultaneous Helium Injection on Defect Cluster Nucleation in Irradiated Metals", J. Nucl. Matls. 86, 565 (1979).

28. M. H. Yoo and L. K. Mansur, "The Inclusion of Mobile Helium in a Rate Theory Model of Void Swelling", J. Nucl. Matls. 86, 571 (1979).

29. E. A. Kenik and E. H. Lee, "Influence of Injected Helium on Phase Instability", Symposium on Irradiation Phase Stability, Fall Meeting AIME Met. Soc., Pittsburgh (Oct. 1980).

30. A. C. Roberts, D. R. Harries, D. R. Arkell, M. A. P. Dewey and J. D. H. Hughes, "Effect of Ytrrium on the Structure and Post-Irradiation Tensile Properties of an Iron-Chromium-Aluminum Alloy", Symposium on Irradiation Effect in Structural Alloys for Thermal and Fast Reactors, San Francisco, 1968, American Society for Testing and Materials, special technical publication No. 457, 313 (1969).

31. R. W. Chickering, R. Bajaj, and J. S. Lally, "A Comparison of the Irradiation Effects on Swelling in Commercial Alloy A-286 and a Simple Fe-25% Ni-15% Cr Gamma Prime Hardened Alloy", Radiation Effects in Breeder Reactor Structural Material, edited by M. L. Bleeberg and J. W. Bennett, (Met. Soc. of AIME, New York, N. Y., p. 405, 1977).

VIII. ACKNOWLEDGMENTS

Deep, heartfelt gratitude is extended to Dr. M. S. Wechsler for his guidance and instruction during the course of my studies and research. His daily exchange of knowledge and edification has made him what I would call a truly remarkable educator. I would like to extend my appreciation to Wes Alexander for his willingness to lend assistance in the myriad of tasks performed during the course of this research, and to acknowledge the cooperation of M. B. Lewis, N. H. Packan, and R. A. Buhl for their help at the Van de Graaff Dual Beam Accelerator at the Oak Ridge National Laboratory and J. J. Laidler and J. L. Straalsund of the Hanford Engineering Development Laboratory for providing the starting alloy stock. I would also like to thank my parents, Mr. and Mrs. C. Irvin Hopson, and my wife, Connie, for their moral support and the United States Army for giving me the time and finances to achieve my educational goals. Finally, I am forever indebted to God, without whom all of this would not have been possible.